

## The effect of turbulent coherent structures in atmospheric flow on wind turbine loads

Dangi, Nirav; Sodja, Jurij; Ferreira, Carlos Simão; Yu, Wei

**DOI**

[10.1016/j.renene.2024.122248](https://doi.org/10.1016/j.renene.2024.122248)

**Publication date**

2025

**Document Version**

Final published version

**Published in**

Renewable Energy

**Citation (APA)**

Dangi, N., Sodja, J., Ferreira, C. S., & Yu, W. (2025). The effect of turbulent coherent structures in atmospheric flow on wind turbine loads. *Renewable Energy*, 241, Article 122248. <https://doi.org/10.1016/j.renene.2024.122248>

**Important note**

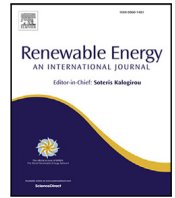
To cite this publication, please use the final published version (if applicable). Please check the document version above.

**Copyright**

Other than for strictly personal use, it is not permitted to download, forward or distribute the text or part of it, without the consent of the author(s) and/or copyright holder(s), unless the work is under an open content license such as Creative Commons.

**Takedown policy**

Please contact us and provide details if you believe this document breaches copyrights. We will remove access to the work immediately and investigate your claim.



# The effect of turbulent coherent structures in atmospheric flow on wind turbine loads

Nirav Dangi<sup>\*</sup>, Jurij Sodja, Carlos Simão Ferreira, Wei Yu

*Delft University of Technology (TU Delft), Aerospace Engineering, Delft, 2629 HS, The Netherlands*

## ARTICLE INFO

### Keywords:

LES  
ABL  
SPOD  
Coherence  
Aero-elastic  
Wind turbine

## ABSTRACT

Large wind turbines face more intricate atmospheric conditions with turbulent coherent structures sized similarly to the rotor diameter, posing loading challenges. The present study assesses twelve distinct wind fields using the Large Eddy Simulations (LES) and International Electrotechnical Commission (IEC) Kaimal model scaled to their LES counterpart. The hub height wind speed in the different cases was set to 8.5 m/s (below-rated), 11.5 m/s (at-rated), and 14.5 m/s (above-rated).

In a previous study, it was found that the unscaled IEC model-based wind field is conservative and scaled IEC model-based wind fields were found to yield different loads than upon use of LES-based wind fields in different atmospheric stability conditions. The present study aims to understand these differences. Utilizing Spectral Proper Orthogonal Decomposition (SPOD), the original wind fields were decomposed and reconstructed to study the influence of large and small coherent structures represented by their distinct frequencies. SPOD analysis was complemented by wind field spectral analysis considering atmospheric surface layer height, integral length scales, and co-coherence estimates.

Integral length scales in the scaled IEC Kaimal model were found to be half of those in unstable atmosphere LES wind fields. The aero-elastic impact on the IEA 22 MW reference wind turbine with a 280 m rotor diameter was evaluated. The analysis reveals that large coherent structures, particularly low-frequency ( $\leq 0.06$  Hz) ones, significantly impact wind turbine loads, contingent upon atmospheric stratification. Compared to the scaled IEC Kaimal model wind field, the maximum tower fore-aft bending moment and the maximum blade root flap-wise bending moment were found to be higher, for example, by 10% and 5% respectively in an unstable atmosphere during below-rated wind turbine operation. In the same scenario, standard deviation of the tower fore-aft bending moment was found to be higher by up to 50% while standard deviation of the blade root flap-wise bending moment was found to be lower by up to 25%. These findings underscore the critical importance of accurately modeling atmospheric turbulence and its coherent structures for more reliable design and operation of large wind turbines.

## 1. Introduction

The process of designing wind turbines follows a structured approach outlined by the International Electrotechnical Commission (IEC) wind turbine design standards [1]. These standards encompass a wide spectrum of wind turbine operation regimes under normal and extreme inflow conditions. Such a structured approach has enabled the development of reliable wind turbines and contributed to the success of the wind energy field. To better adapt to the future wind energy deployment goals, one of the key challenges raised by the design standards is the wind inflow criteria [2]. This challenge stems from the continuous increase in wind turbine size with >15 MW wind turbines already deployed and some in stages of development. These wind turbines have rotor diameters exceeding 250 m, increasingly subjecting

them to the more intricate dynamics of the atmospheric boundary layer (ABL), above the atmospheric surface layer (ASL).

It has been noted in the article [2] on grand challenges for future wind turbine systems that an especially significant opportunity for improvement in the standards is related to the two spectral models allowed in the IEC design standards. These are the Mann Turbulence model [3] and the Kaimal model [4,5] with Davenport's exponential decay model [6]. The latter is an empirical model which, among other parameters, characterizes the coherence (defined below) of the wind field based on the exponential decay model. In contrast, the Mann model is more intricate, utilizing the spectral tensor to create wind fields that are more physically realistic. These models were developed with small turbines in mind and for flow over flat terrain in neutral

<sup>\*</sup> Corresponding author.

*E-mail address:* [n.s.dangi@tudelft.nl](mailto:n.s.dangi@tudelft.nl) (N. Dangi).

atmospheric conditions. The spatial and temporal distribution of the turbulence, represented by coherence, is inconsistently modeled by the two. For instance, the authors in [7] found that for vertical separations, the co-coherence with the Mann model was higher than with the Kaimal model at small wavenumbers. Hence, it is necessary to refine and evolve these existing models to ensure their suitability and enhance load predictions for current and forthcoming large wind turbines in varied atmospheric conditions.

Spatial and temporal scales of motion can be comprehended utilizing space–time correlation and coherence. The former measures the correspondence of fluctuations at two points over time. The latter describes the relationship between signal in the frequency domain. The theory related to the wind-induced response of wind turbines can be traced back to the 1960s [8]. The effect of atmospheric stability on the coherence has been investigated in, for example, [9–11].

Focusing on recent literature, the authors of [12] investigate the coherent structures (“connected, large-scale turbulent fluid mass with a phase-correlated vorticity over its extent” [13]) in the wind fields generated by the use of the Mann and the Kaimal model. Their study was motivated by an earlier study in which they found the fatigue life for a floating spar wind turbine to be sensitive to the choice of turbulence model. Using proper orthogonal decomposition (POD), they find that the Mann turbulence model generates coherent structures that stretch in the horizontal direction for the longitudinal component. In contrast, the structures found in the Kaimal model are more random in their shape. Additionally, in [14], it was noted that the Mann modes seem to be stretched in the lateral direction, whereas Kaimal is more centered around the hub.

In [15], the authors investigate the performance of the Mann model for impact on the response of a bottom-fixed wind turbine. They set the inputs of the Mann model to site-specific wind spectra of one hour of measurements in neutral atmospheric conditions. They find that the Mann model does not reach the high energy levels of measurements at low frequencies. The Mann model with site-specific inputs was found to match more closely at low frequencies but not at high frequencies. The response at low frequencies ( $<0.1$  Hz) was found to have major impact on total damage equivalent moments of the tower bottom bending fore–aft moment. Such observation was also made in [16]. Their analysis of coherent structures showed that similar vertical coherence was observed for the Mann model with and without site-specific inputs. No direct conclusion about the realism of the lateral coherence could be made because of no measurements for laterally separated points. In general, the need for accurate lateral coherence modeling was stressed, especially for low frequencies.

In [14], the authors perform a set of simulations using the Mann and Kaimal model, Large-eddy simulations (LES) and measurements. Their analysis focused on scales relevant for a 10 MW wind turbine with a rotor diameter of 180 m and a hub height of 119 m. Their study included assessing only the different wind fields and not the impact on the wind turbine. Among others, the spectral characteristics of the different wind fields were presented. Coherent structures in the unstable atmosphere were found to be larger than in the neutral and stable ones. More significant coherent structures were also found in the unstable atmosphere, which was concluded on the basis of the energy content of the first POD mode. As expected, the Mann and Kaimal models were found to represent wind field characteristics in neutral stratification better than in stable and unstable stratification.

The study in [17] assesses the impact of different wind fields on a 6 MW spar floating offshore wind turbine. Their analyses reveal that wind fields generated by both Mann and Kaimal models lead to over-prediction of fatigue loading in high-wind scenarios and under-prediction in low-wind scenarios, compared to LES wind fields. In line with other literature, they mention the trend of simulated fatigue loads in relation to the spatial coherence in the wind field. Both stochastic turbulence models were found to over predict fatigue loading in high-wind scenarios and under predict it when the wind speed is low.

However, detailed studies isolating the impacts of different coherent structures on the wind turbine loads are still scarce. Two articles that may be considered to provide such a study can be found in [18,19].

The study in [18] assesses the impact of different coherent structures on the global response of a 5 MW floating wind turbine. Their methodology involved using POD on the wind fields generated by the Mann and the Kaimal models and reconstructing wind fields with different coherent structures. Their reconstructed wind fields had energy contents of 20%, 40–50% and 60–80%, depending on the wind speed, compared to the original wind field. Adding to the body of literature, their results highlight the different results obtained due to the choice of the turbulence model. Moreover, they find that the majority of the surge and pitch response of the turbine could be related to the first POD mode, implying a low-frequency mode. However, it should be noted that the temporal coefficients of spatial POD modes may contain a mix of frequencies [20]. The differences in yaw responses were found to be due to the POD modes representing 45% of energy in comparison to the original wind field. In a recent article, the authors of [19] use POD in a similar manner to assess the performance and wake of a scaled wind turbine. They also assess the impact of the coherent structures on the thrust and power of a 2.5 MW wind turbine in a neutral atmosphere.

A recent investigation conducted by [21] focuses on evaluating the impact of integral length scale (a parameter representative of the average size of the largest energy-containing turbulent eddies) on the loads experienced by a 15 MW wind turbine. The study employs LES to generate five ABL flows with varying integral length scales and atmospheric stability conditions (neutral and unstable), maintaining a mean hub height wind speed of 8 m/s, corresponding to wind turbine operation at below-rated capacity. The LES-generated wind fields were dissected into mean and turbulent components. Turbulent fluctuations were scaled to ensure consistent turbulence intensity across all cases. However, they note that in real-world scenarios, atmospheric stability, integral length scales, turbulence intensity, and mean wind speed are coupled and interact in complex ways. To examine the influence of integral length scale, the study employs three types of decomposed inflow wind fields: mean shear plus turbulence, mean shear alone, and mean uniform plus turbulence. These wind fields are then input into standalone OpenFAST simulations with active rotor speed control but without pitch and yaw control. The findings reveal that when the integral length scale is larger than the rotor diameter ( $D$ ), up to  $1.7D$ , there is an increase in thrust, blade root shear, and flap-wise moment. Consistent with prior research, turbulence was found to impact the wind turbine loads profoundly. Their study did not aim to evaluate the influence of various coherent structures and did not include an analysis of stable ABL and Kaimal or Mann model-based wind fields. They suggest that future studies should explore the effects of integral length scale in scenarios of wind turbine operation at-rated and above-rated capacities. Lastly, in a recent aero-elastic study conducted by the authors [22] using the IEA 22 MW wind turbine, it was found that the unscaled IEC Kaimal model-based wind field is conservative, and that scaled IEC model-based wind fields yield different loads compared to LES-based wind fields under various atmospheric stability conditions. In the present study, these differences are further investigated.

Through this literature review, it becomes apparent that there is a need to improve turbulence models within the current IEC design standards. This improvement is essential for better suitability to the conditions faced by large wind turbines situated well above the atmospheric surface layer, particularly in offshore environments, frequently characterized by non-neutral conditions [23–25].

The existing literature presents numerous discrepancies in the results due to the choice of turbulence models. The coherent structures have been found to be a key driver for these discrepancies. However, a comprehensive investigation that conducts a detailed analysis of the spatio-temporal characteristics of the wind field and understands its effects on wind turbine loads is yet to be undertaken. This gap in the literature becomes particularly pronounced when considering the

combined analysis in a non-neutral atmosphere. The present study aims to fill this gap in the literature by conducting a systematic study on the impact of coherent structures on aero-elastic loads. The study presents both the influence of different atmospheric stability on coherent structures and the effect of various coherent structures on aero-elastic loads. Furthermore, the existing literature is intended to be enhanced by presenting spatio-temporal characteristics of wind fields at scales relevant for the very large wind turbines. Further, the present study uses spectral POD rather than the classical POD. This approach allows for the extraction of modes with specific frequencies. A similar approach to study the different coherent structures using dynamic mode decomposition can be found in [26].

The structure of this article is as follows: Section 2 provides a brief theoretical background on the methods utilized in this study. Next, Section 3 provides the simulation setup. Later, the results are discussed in two subsections; Section 4.1 provides a breakdown of the different coherent structures in different atmospheric conditions, following which Section 4.2 presents the aero-elastic impact of the different coherent structures in terms of several quantities of interest. Lastly, concluding remarks and recommendations for further work are placed in Section 5.

## 2. Methods

The v1.0.1 IEA 22 MW reference wind turbine (RWT) [27,28], with a hub height of 170 m and a rotor diameter of 280 m was chosen for this study. The wind turbine operation during below, at, and above-rated wind speed conditions was analyzed. Twelve wind fields with different atmospheric conditions were considered for analysis, generated using LES (employing NREL SOWFA<sup>1</sup> [29] coupled with OpenFOAM [30]) and the Kaimal model (utilizing NREL TurbSim [31]). The original wind fields and wind fields with different turbulence energy contributions reconstructed using SPOD were imported to standalone blade element momentum (BEM) theory simulations in the widely used aero-elastic tool NREL OpenFAST<sup>2</sup> [32]. The coming subsections provide a theoretical background on the methods used in this study.

### 2.1. Large eddy simulations

The scope of this article is to utilize NREL SOWFA to generate LES-based precursor ABL wind fields. Standalone BEM theory simulations were run with wind fields from LES ABL precursors. NREL SOWFA [29] is a widely used open-source high-fidelity tool that is a set of computational fluid dynamics (CFD) solvers, boundary conditions, and turbine models. SOWFA simulates the ABL and is coupled to OpenFOAM [30] and NREL OpenFAST [32]. ABL is the bottom 0.3 km to 3 km of the troposphere and is often turbulent and varies in thickness in space and time. The conditions in ABL are determined by the effects of the Earth's surface, which slows the wind due to surface drag, warms the air during daytime and cools it at night, and changes in moisture and pollutant concentration [33]. Below is a short description of the LES solver, in line with nomenclature from [34].

The spatially filtered, incompressible Navier–Stokes equations to give the resolved-scale (large-eddy scale) dynamics of fluid flow incorporate the filtered continuity equation as shown in Eq. (1).

$$\frac{\partial \bar{u}_j}{\partial x_j} = 0 \quad (1)$$

where the overbar denotes spatial filtering and  $\bar{u}_j = u_j - u'_j$  is the resolved-scale velocity vector, which is the instantaneous velocity vector,  $u_j$ , minus the subfilter-scale (SFS) velocity vector,  $u'_j$ . The filtered

<sup>1</sup> NREL SOWFA-6 was used in this study and is hereafter referred to as NREL SOWFA.

<sup>2</sup> NREL OpenFAST v3.5.1 was used in this study and is hereafter referred to as NREL OpenFAST.

momentum equation is shown in Eq. (2)

$$\begin{aligned} \frac{\partial \bar{u}_i}{\partial t} + \frac{\partial}{\partial x_j} (\bar{u}_j \bar{u}_i) = & \underbrace{-2\epsilon_{ijk}\Omega_3 \bar{u}_k}_{\text{I}} - \underbrace{\frac{\partial \bar{p}}{\partial x_i}}_{\text{II}} - \underbrace{\frac{1}{\rho_0} \frac{\partial}{\partial x_i} \rho_0(x, y)}_{\text{III}} \\ & - \underbrace{\frac{\partial \tau_{ij}^D}{\partial x_j}}_{\text{IV}} + \underbrace{g \left( \frac{\bar{\theta} - \theta_0}{\theta_0} \right) \delta_{i3}}_{\text{V}} + \underbrace{\frac{1}{\rho_0} F_i^T}_{\text{VI}} \end{aligned} \quad (2)$$

Term I is the Coriolis force due to planetary rotation, and  $\epsilon_{ijk}$  is the alternating tensor. The rotation rate vector is given by  $\Omega_j$ , as,  $\Omega = \omega[0, \cos(\phi), \sin(\phi)]$ , where  $\omega$  is the planetary rotation rate and  $\phi$  is the latitude. This study used a latitude of 52.8°, representing the Dutch North Sea [35]. Term II is the gradient of the modified pressure variable. Term III represents the background driving pressure gradient. Term IV is the divergence of the deviatoric part of the fluid stress tensor. The stress is composed of a viscous and an SFS part. The one equation eddy-viscosity SFS model from [36,37] was used. Term V is used to model buoyancy effects using the Boussinesq approximation. Term VI accounts for other density normalized forces, if relevant, for example, the body force field exerted in the case of an actuator line turbine model. The equation for the transport of resolved potential temperature is shown in Eq. (3).

$$\frac{\partial \bar{\theta}}{\partial t} + \frac{\partial}{\partial x_j} (u_j \bar{\theta}) = - \frac{\partial q_j}{\partial x_j} \quad (3)$$

Here  $q_j$  represents the flux of temperature by viscous and SFS effects.

### 2.2. Spectral proper orthogonal decomposition

Spectral Proper Orthogonal Decomposition (SPOD) is a frequency-domain adaptation of Proper Orthogonal Decomposition (POD). It calculates modes by estimating the eigenvectors of the cross-spectral density (CSD) matrix. SPOD generates a series of orthogonal modes at each frequency, ordered by energy. SPOD stands out from classical POD by featuring modes that vary across space and time, being orthogonal under a space–time inner product rather than solely in space [20]. This unique characteristic makes them particularly effective in capturing spatio-temporal coherence within the data [38]. A short overview of the method (following [39]) with mathematical principles as initially outlined by Lumley in the 1960s [40,41] is provided here.

Let  $q_i = q(t_i)$  be a multi-dimensional fluctuating flow field obtained by subtracting the temporal mean  $\bar{q}$ . This matrix can be written in a snapshot form as  $Q = [q_1, q_2, \dots, q_n]$ . Here  $i = 1, \dots, n_t$ , and the length  $n$  corresponds to the number of variables times the number of grid points.

SPOD specializes in POD to analyze turbulent flows or statistically stationary processes. It aims to identify optimal modes in the context of the space–time inner product (Eq. (4)).

$$\|q\|_{x,t}^2 = \langle q, q \rangle_{x,t} = \int_{-\infty}^{\infty} \int_{\zeta} q^*(x, t) q(x, t) dx dt. \quad (4)$$

Note that a term  $W(x)$ , a positive-definite Hermitian matrix to account for component-wise weights is dropped here to maintain uniform contribution of all components.  $\zeta$  represents the spatial domain of interest and  $(.)^*$  denotes the complex conjugate. In the case of SPOD, the POD eigenvalue problem is solved for the Fourier transformed two-point space–time correlation matrix (CSD matrix). The Welch [42] method was followed to estimate the CSD. 7 segments with 50% overlap leading to 13 blocks were used. A hamming window was applied to the overlapping blocks to reduce spectral leakage. The subsequent matrix containing all realizations of the Fourier transform at the  $l$ th frequency can be written as  $\hat{Q}_l = [\hat{q}_l^{(1)}, \hat{q}_l^{(2)}, \dots, \hat{q}_l^{(n_{blk})}]$ . From this form, the SPOD modes,  $\Phi$ , and associated energies,  $\lambda$ , can be computed as the eigenvectors and eigenvalues of the CSD matrix  $S_l = \hat{Q}_l \hat{Q}_l^*$ . More economically, an analogous eigenvalue problem can be solved for the coefficients  $\psi$  that expand the SPOD modes in terms of the Fourier

realizations, as shown in Eq. (5).

$$\frac{1}{n_{blk}} \hat{Q}_l^* \hat{Q}_l \Psi_l = \Psi_l A_l \quad (5)$$

In terms of the column matrix  $\Psi_l = [\psi_l^{(1)}, \psi_l^{(2)}, \dots, \psi_l^{(n_{blk})}]$ , the SPOD modes at the  $l$ th frequency are recovered as formulated in Eq. (6).

$$\Phi_l = \frac{1}{\sqrt{n_{blk}}} \hat{Q}_l \Psi_l A_l^{-1/2} \quad (6)$$

The matrix of SPOD energies  $A_l = \text{diag}(\lambda_l^{(1)}, \lambda_l^{(2)}, \dots, \lambda_l^{(n_{blk})})$ , is arranged in descending order of energies. The SPOD modes are contained in  $\Phi_l = [\phi_l^{(1)}, \phi_l^{(2)}, \dots, \phi_l^{(n_{blk})}]$ .

One may perform the inversion of the SPOD solution to reconstruct the original data in its entirety or desired parts. This study's reconstruction was done to generate wind fields with the desired frequency content. The frequencies of interest were chosen as 0.01–0.03 Hz, 0.01–0.06 Hz and 0.06–0.25 Hz. The reasoning is to isolate the effect of different coherent structures: the lower-frequency coherent structures represent larger eddies, while the higher-frequency coherent structures represent smaller eddies. Given the novelty of the use of SPOD in this study, the ranges were established here to account for approximately 50%, 20% and 10% of the total turbulence energy, respectively. Additionally, the established ranges resemble structures of high coherence, intermediate coherence and least coherence between two points (see Fig. 6). The reconstruction was done in the frequency domain, and the approach provided in [43] was followed. The original realizations of the Fourier transform at each frequency can be reconstructed as  $\hat{Q}_l = \Phi_l A_l$ , where  $A_l$  is the matrix of expansion coefficients  $A_l = \sqrt{n_{blk}} A_l^{1/2} \Psi_l^* = \Phi_l^* \hat{Q}_l$ . Next, the Fourier-transformed data of the  $k$ th block can be reconstructed as shown in Eq. (7)

$$\hat{Q}^{(k)} = \left[ \left( \sum_i a_{ik} \phi^{(i)} \right)_{l=1}, \left( \sum_i a_{ik} \phi^{(i)} \right)_{l=2}, \dots, \left( \sum_i a_{ik} \phi^{(i)} \right)_{l=n_{ff}} \right] \quad (7)$$

Lastly, the original data in the  $k$ th blocks  $Q^{(k)}$  was recovered using the window weighted inversion (see Appendix A of [39]) formulated in Eq. (8).

$$q_j^{(k)} = \frac{1}{w(j)} \mathcal{F}^{-1} \{ \hat{q}_j^{(k)} \} \quad (8)$$

Regarding the reconstruction of wind fields with specific frequency contents, a band-pass filter was used only to retain the expansion coefficients of the desired frequencies. All the modes at the desired frequency were used for reconstruction. An example visualization of the SPOD results and reconstruction is shown in Appendix A.

### 2.3. Wind field characteristics

In addition to the SPOD analysis and reconstruction of wind fields, a quantification of the spectral characteristics of the wind was carried out to compare further the IEC Kaimal model-based and LES wind fields.

The co-coherence, quad-coherence, and root-coherence were computed (Eq. (9), where  $f$  is the frequency). These refer to the real part, imaginary part, and amplitude of a two-point cross-spectrum, respectively, normalized by the product of power spectra for each point [44].

$$\text{coh}(f) = \underbrace{\frac{\text{Re} [S_{xy}(f)]}{\sqrt{S_{xx}(f)S_{yy}(f)}}}_{\text{co-coherence}} + i \underbrace{\frac{[S_{xy}(f)]}{\sqrt{S_{xx}(f)S_{yy}(f)}}}_{\text{quad-coherence}} \quad (9)$$

The IEC Kaimal model ignores the quad co-coherence. Hence, only the co-coherence is presented and discussed here as a comparison. The IEC guideline [1] specifies the use of the Kaimal auto spectrum with the modified Davenport's exponential coherence model for the longitudinal

velocity component as shown in Eq. (10).

$$\text{coh}(r, f) = \exp \left[ -12 \left( (fr/V_{hub})^2 + (0.12r/L_c)^2 \right)^{0.5} \right] \quad (10)$$

In Eq. (10),  $r$  represents the length of the projection of the vector that separates the two points onto a plane that is perpendicular to the average direction of the wind,  $L_c$  is the coherence scale parameter given as 8.1 times the longitudinal turbulence scale parameter which is suggested to be 42 m for hub heights  $\geq 60$  m, and  $V_{hub}$  is the velocity at the hub height. Assessing the co-coherence allows one to get information about the phase of the two signals. A negative co-coherence indicates an out-of-phase relationship between the two signals, of phase relationship between the two signals (here, the velocity components at different location(s)). Additionally, the integral length scales in the stream-wise and span-wise directions were calculated with the formulations described in [45] and shown in Eq. (11).

$$L_i^x = \bar{U} \cdot \int_{t=0}^{t(R_i(t)=0)} R_i(t) dt \quad (11)$$

$$L_i^y = \int_0^{+\infty} R_i(\tau), d\tau$$

The stream-wise integral length scale is denoted by  $L_i^x$  and the span-wise integral length scale is denoted by  $L_i^y$ . Here,  $i$  is used to denote the three wind speed components,  $R_i$  is the single-sided auto-covariance function of the fluctuating wind velocity, and  $\tau$  denotes the time lag.  $L_i^x$  was computed on the basis of the integration up to the first zero-crossing [46] of  $R_i$ .  $L_i^y$  was computed by an integral of an exponential decay function to approximate the correlation coefficients as a function of span-wise separation [45].

As noted previously, the IEC Kaimal and Mann models are intended for use in the atmospheric surface layer in a neutrally stratified atmosphere. However, the present study incorporates stable and unstable atmospheric boundary layers. Hence, it is relevant to assess the atmospheric surface layer height in the wind fields generated in the present study to highlight wind field characteristics not captured by the IEC models. Recall that the atmospheric surface layer is the first 10–20% of the atmospheric boundary layer [33], where the turbulent fluxes may be approximated as constant. To get a more comprehensive estimate of the ASL height, the friction velocity variation against altitude was analyzed. Following [47], the friction velocity ( $u_*$ ) was estimated as shown in Eq. (12).

$$u_* = \left( \overline{u'w'^2} + \overline{v'w'^2} \right)^{1/4} \quad (12)$$

The altitude at which the friction velocity was found to decrease sharply was chosen as the ASL height [48] (shown in Fig. A.18), and the values are discussed later and tabulated in Table 1.

## 3. Simulation set-up

### 3.1. Wind field generation

The simulations involved 12 distinct wind fields, with 9 LES-based wind fields and 3 wind fields employing the IEC Kaimal model. The LES configuration comprised two stages. A precursor ABL was initially generated within an empty domain, illustrated as solid black lines in Fig. 1. To achieve a fully developed ABL, this precursor simulation was run for 20 000 s for cases with neutral and unstable ABL and 25 000 s for cases with stable ABL [49]. This disparity in duration aimed to accommodate more complex development of shear, leading to low-level jet-like scenarios. An adjustable time-step was used in these simulations based on free-stream wind speed based Courant–Friedrichs–Lewy (CFL) number [50] being at maximum, 0.75; leading to a time-step between 0.3 s to 0.5 s, depending on the mean free-stream wind speed.

Subsequently, in all cases, the next 700 s were used for actuator line model (ALM)-based LES was executed. The wind fields were sampled in the ALM-LES setup. The horizontal homogeneity and shear profile development were examined within the 700 s to confirm the developed

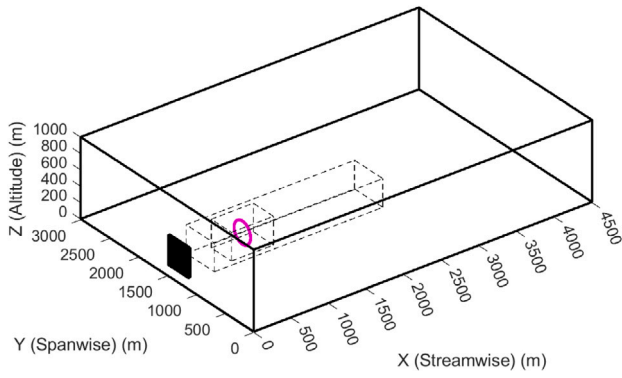


Fig. 1. 3-D view of the domain. The dotted rectangles represent two refinement regions. The sampling plane is denoted as a filled black rectangle at an upstream distance of 3D. The rotor is denoted by a magenta circle.

ABL and variation within acceptable bounds. A sampling plane with probes was employed to record velocity at a 3D upstream distance (shown in Fig. 2). This distance was deemed sufficient to sample velocity without the influence of the wind turbine induction zone (shown in Fig. A.19). The ALM-LES domain differed from the precursor domain only in utilizing two refinement boxes, delineated by dotted lines in Fig. 1. The global mesh sizing was 10 m (in line with existing literature [21,51,52]), and the local mesh size in the refinement boxes 1 and 2 was 5 m and 2.5 m, respectively. These refinement boxes did not intersect with the sampling plane; hence, velocity probing occurred within cells isotropically sized 10 m. The wind field sampled here was later used for standalone BEM simulations.

In regards to the result sensitivity with the grid size, it may be noted that the focus of this study is on large-scale structures instead of the high-frequency small-scale structures. A sensitivity study of ABL-LES can be found in [53], highlighting the differences in atmospheric characteristics. In line with their recommendations, the grid sizing in the neutral and unstable ABL LES of this study can be considered well resolved. The grid sensitivity of the stable ABL LES on the results of this study are provided in Appendix D. The results indicate marginal differences (up to  $\pm 4\%$ ) in the load channels of interest, hence, to ensure reasonable computational costs of the three stable LES, the grid size is chosen as 10 m. The velocity probing sampling frequency was set to correspond to once every 5 time steps of the simulation, which lead to a sampling frequency of approximately 4 Hz. The sampling probes are shown in Fig. 2. The energy spectra of the wind field was analyzed to chose a reasonable cut-off frequency for the further analysis. As in one of the approaches in [53], the energy spectra was plotted and the inertial subrange was identified using the Kolmogorov's  $-5/3$  slope, shown in Fig. A.14. This resulted in the choice of 0.25 Hz as the cut-off frequency.

Regarding the precursor ABL parameters, first, the surface roughness was chosen based on the implicit Charnock equation:

$$z_0 = \frac{A_c}{g} \left[ \frac{\kappa V_{hub}}{\ln \frac{z_{hub}}{z_0}} \right]^2 \quad (13)$$

In the above equation,  $A_c$  is Charnock's constant and is recommended to be 0.011 for open sea [54],  $\kappa = 0.4$  is von Karman's constant,  $g = 9.81 \text{ m/s}^2$  is acceleration due to gravity and  $z_{hub} = 170 \text{ m}$  is the hub height of the IEA 22 MW wind turbine. Using a hub height velocity of  $11.5 \text{ m/s}$ , numerically solving the above equation yields  $z_0 = 0.0001 \text{ m}$ . This input surface roughness was set the same for all the simulations. The Schumann-Grotzbach wall shear stress model was used on the lower surface with the Monin-Obukhov similarity theory [55] based on the calculation of surface friction velocity. For the upper boundary, the conditions were set to represent the geostrophic wind; wall shear

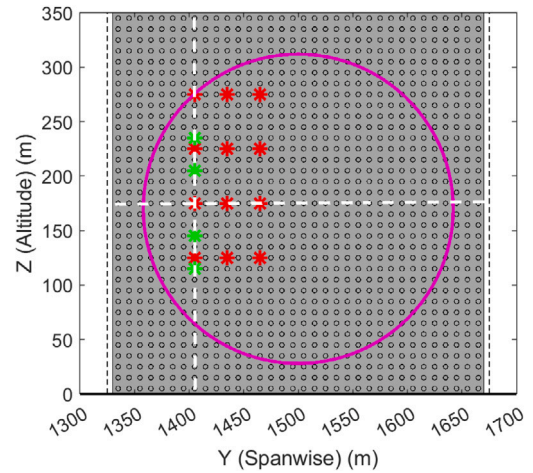


Fig. 2. 2-D view of the domain in the Y-Z plane. The probes are shown as black hollow circles. The rotor is denoted by a magenta circle. The white dotted line represents a line along the base location chosen for coherence analysis. The red asterisks (each separated by 50 m) and green asterisks (each separated by 30 m) are the points chosen for coherence analysis of laterally and vertically separated points, respectively.

stress was set to zero, and the slip condition for velocity (zero perpendicular velocity) was specified. The reference wind speed was set as the corresponding value for the different cases at hub height, driven by a constantly adjusting pressure gradient.

Next, the Coriolis parameter was calculated using a latitude of  $52.8^\circ$ , representative of the Dutch North Sea [35]. A capping inversion at 500 m was set for all simulations. The reference potential temperature was set as 300 K. Within a 100 m inversion width, the potential temperature was set to vary from 300 K to 305 K. Above the inversion layer, a potential temperature gradient of  $0.003 \text{ K/m}$  was specified [34].

On the lower boundary, a temperature flux of  $-0.02 \text{ K/m/s}$  in the altitude direction was applied for the unstable ABL simulations, while  $0.02 \text{ K/m/s}$  was applied for the stable ABL simulations [56]. On the upper boundary, the temperature flux was set as zero. The precursor ABL simulation domain's other faces (north, east, south, and west) were set to cyclic boundary conditions. The simulations were run using the DelftBlue [57] and the Dutch national supercomputer, Snellius. Each precursor ABL simulation had a wall clock time between 30 to 72 h, depending on the case and number of cores used.

The lower fidelity wind field, the Kaimal model-based inflow profiles were generated using TurbSim [31]. The Kaimal model-based wind fields used in this study differ from the IEC guidelines in two ways. First, a power law wind shear exponent ( $\alpha$ ) of 0.11 was used, as this value matched the neutral atmosphere LES wind profiles. The IEC offshore guideline specifies  $\alpha = 0.14$ . Second, the turbulence intensity was scaled down to match the turbulence intensity of the corresponding LES cases, which have a hub height turbulence intensity close to 5%. For both methods, a hub height wind speed of  $8.5 \text{ m/s}$  was selected to represent wind turbine operation below-rated conditions. Next, a hub height wind speed of  $11.5 \text{ m/s}$  was chosen, corresponding to near-rated conditions for wind turbine operation. Lastly, a hub height wind speed of  $14.5 \text{ m/s}$  was selected to represent the above-rated wind turbine operation.

### 3.2. Inflow profiles

The planar and temporally averaged inflow profiles for the distinct wind fields generated in this study are presented and discussed here. Fig. 3(a) displays the inflow profiles for the scenario with a hub height wind speed of  $8.5 \text{ m/s}$ . The results show a stable atmosphere with high wind shear, an unstable atmosphere with low wind shear, and

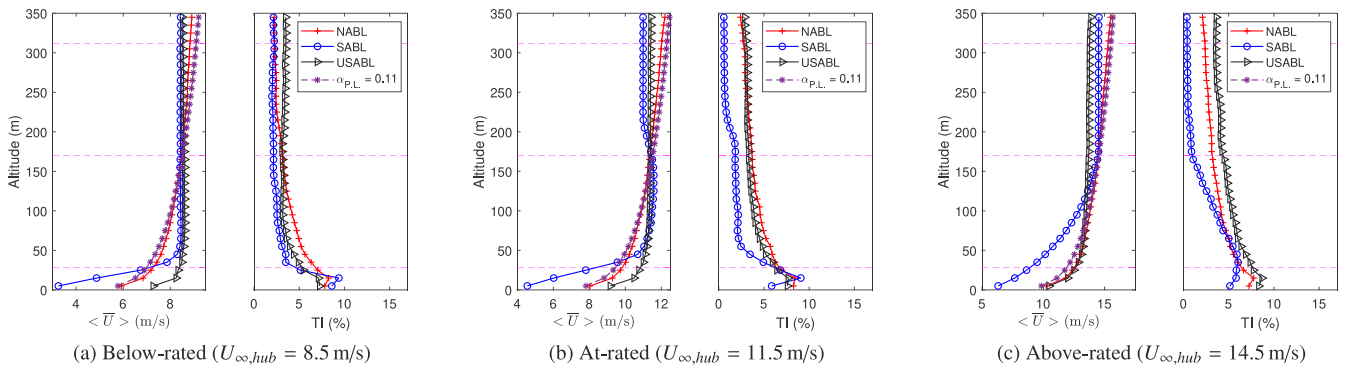


Fig. 3. Inflow profiles of planar averaged U component of wind speed and its turbulence intensity (TI), for different atmospheric conditions. The magenta lines indicate the rotor tips and hub height.

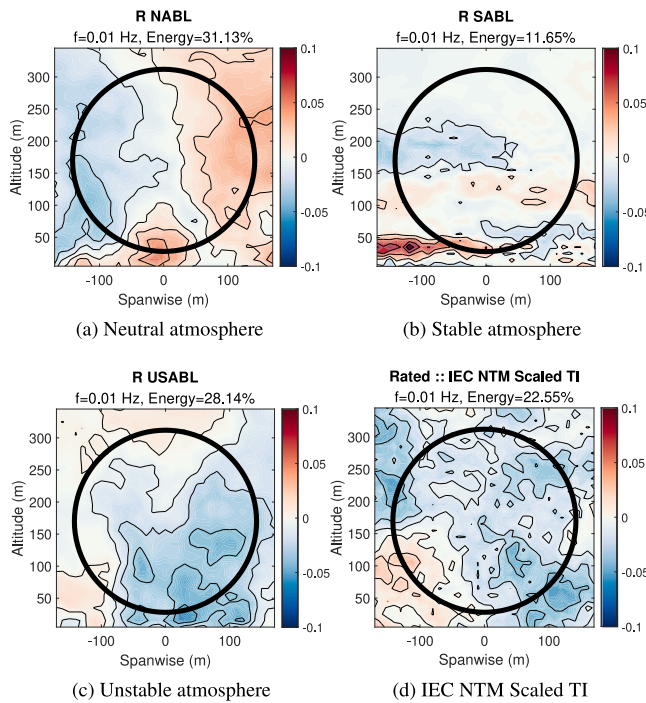


Fig. 4. SPOD mode 1 with frequency 0.01 Hz in the at-rated scenario.

a neutral atmosphere with a power law wind shear of approximately 0.11. Next, for the at-rated scenario, as shown in Fig. 3(b), the stable atmosphere is characterized by complex wind shear and a low-level jet, with a wind speed peak occurring near the wind turbine hub height. A minor overshoot in turbulence at low altitudes is evident in Fig. 3(b), possibly due to the shallow boundary layer and low-level jet in that scenario. Furthermore, the stable atmosphere is typically influenced by small-scale processes [58], and it may be possible that the grid resolution in this study was coarse to resolve these scales accurately or that the SFS model did not adequately capture these features at low altitudes. However, given the LES energy spectra and the cut-off frequency chosen in this study (Fig. A.14), this effect is deemed to not affect the wind field spectral analysis conducted in this study. Furthermore, it is known that the higher frequency region has minimal impact on loads [14], hence, it does not affect the aero-elastic analysis of the wind turbine as well. Both the unstable and neutral atmospheres in the at-rated scenario, as well as those in the above-rated scenario (Fig. 3(c)), exhibit characteristics similar to those observed in Fig. 3(a). In particular, in Fig. 3(c), the wind speed in the stable atmosphere plateaus above the rotor hub height. Similar profiles are also seen in

a numerical study by the authors of [59]. In general, a low turbulence intensity trend is observed, which can be attributed to the low surface roughness and high altitudes. Exceptionally low turbulence intensities (1%) at higher altitudes in stable atmospheres, a finding also noted in the literature, such as in [60].

### 3.3. Aero-elastic simulations

The wind turbine aero-elastic simulations were performed using NREL OpenFAST [32], a widely used open-source aero-hydro-servo-elastic tool. Stand-alone OpenFAST simulations were run with the wind field output from the sampling probes from LES. The blade element momentum theory along with the time-dependent Øye’s dynamic inflow model (see [61] for details) was used for the aerodynamic calculations. The Beddoes–Leishman dynamic stall model with the Minnema/Pierce variant (see [62] for details) was used for incorporating the effects of dynamic stall. The module ElastoDyn was used for the structural calculations. This module uses the Euler–Bernoulli beam and does not incorporate a blade-torsion degree of freedom. The NREL ROSCO controller [63] was used to control among other parameters, the wind turbine blade pitch and rotational speed.

## 4. Results

### 4.1. Impact of atmospheric stability on wind field spectral characteristics

Here, the characteristics of the 12 different wind fields are presented and discussed. This is aided by visualizing the different coherent structures obtained by utilizing SPOD, by analysis of the lateral and vertical co-coherence and integral length scales. The SPOD aided coherent structure visualizations are shown below for the cases with a hub height wind speed of 11.5 m/s, corresponding to the rated conditions for the wind turbine. Due to the similarity between the different cases, the remaining visualizations are provided in Appendix B. The co-coherence and integral length scales are estimated for all the different inflow conditions.

First, focusing on the SPOD results, Fig. 4 shows the coherent structures with a frequency of 0.01 Hz in the different wind fields with a hub height wind speed of 11.5 m/s. It can be noted that the stable atmosphere has prominent laterally stretched structures, while the other wind fields have diagonally or vertically stretched structures (as also reported in, for example, [64]). The lack of vertical mixing and the shallow boundary layer in a stable atmosphere are among the factors leading to these layered, wave-like structures. The authors of [65] use flow visualization techniques and find such quasi-horizontal modes in a very stable atmosphere. The study in [66] also reports wave-like activity on the top of a stable surface layer. Next, it can be seen in Fig. 4(d) that the Kaimal model does not account for large coherent structures at this rotor scale. This characteristic may have

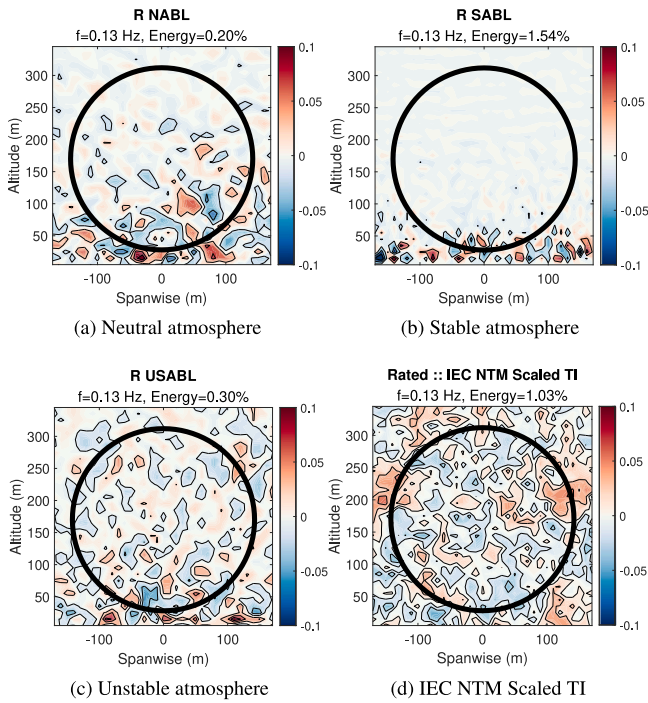


Fig. 5. SPOD mode 1 with frequency 0.13 Hz in the at-rated scenario.

Table 1

Estimated atmospheric surface layer height in different LES wind fields. AR, BR, R refer to the cases with above-rated, below-rated, and rated wind turbine operation, respectively.

Scenarios	Atmospheric surface layer height
AR NABL	125 m
AR SABL	105 m
AR USABL	135 m
BR NABL	145 m
BR SABL	25 m
BR USABL	115 m
R NABL	135 m
R SABL	25 m
R USABL	135 m

been adequate for smaller rotors but may not allow for an accurate representation of the spatio-temporal resolution across the diameter of the larger rotors. A similar observation can be made for Figs. B.20 and B.24 for the 0.01 Hz coherent structures in below and above-rated scenario. Furthermore, it can be said that the low-frequency SPOD modes in LES-based wind fields have a higher energy content than the scaled IEC Kaimal model-based wind field. Two exceptions to this trend are the stable atmosphere cases in Figs. 4(b) and B.20(b). Next, Fig. 5 provides visualization of the higher-frequency, low-energy coherent structures. These structures are small and will impact wind turbine loads locally and have minimal global impact [67].

Further insights into the different coherent structures are provided using co-coherence analysis (Eq. (9)). Below, all estimates of co-coherence are provided using the Welch method [42] with 7 segments, 50% overlap, and a Hann window function. A simple moving average filter over 5 points smoothed the resulting co-coherence estimates.

The co-coherence in the different wind fields was compared with the IEC coherence function (Eq. (10)). As previously noted, the IEC coherence function is designed for neutral stratification within the atmospheric surface layer (ASL). Hence, it is worthwhile to first estimate the ASL height. This study estimated the ASL height by analyzing the friction velocity (Eq. (12)) variation against altitude. The estimate of ASL height helps realize the altitudes above which the wind field

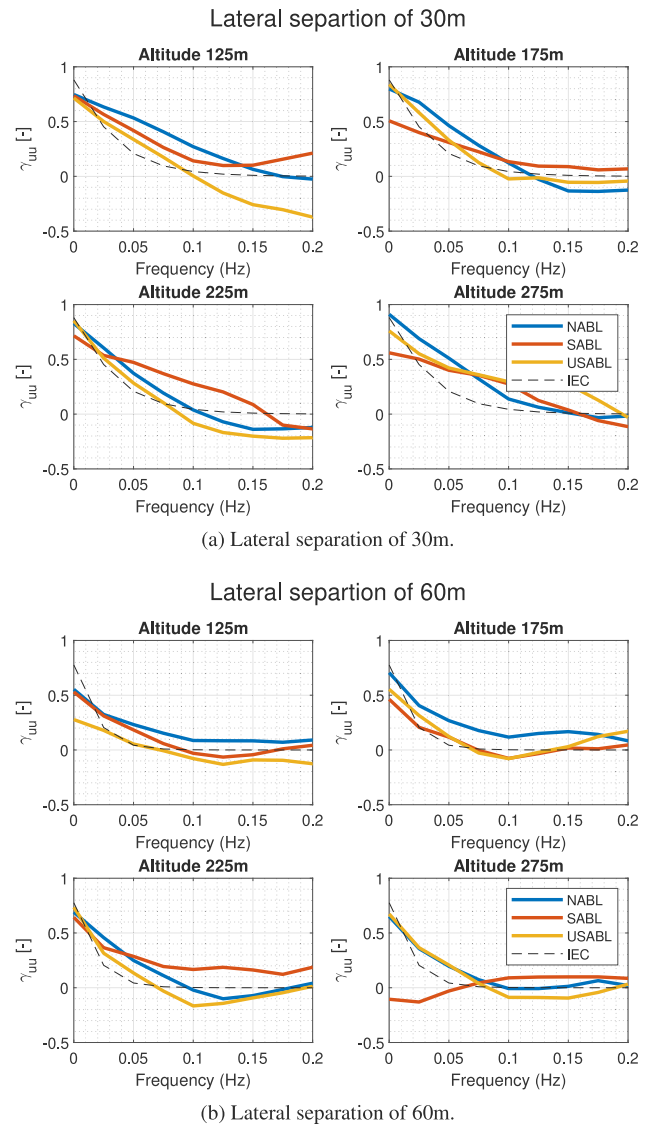


Fig. 6. Co-coherence for the U component at different lateral separations in the at-rated scenario. The measurement points are shown in Fig. 2.

characteristics are not inherently represented by the IEC coherence function and need better modeling for large rotors. The ASL heights for the different wind fields are tabulated in Table 1.

It can be observed that the stable atmospheres have a very shallow ASL, especially in the below and at-rated scenarios, which have an ASL height of 25 m. Generally, it has been found that unstable atmospheres have a higher ASL height, as anticipated. The neutral and unstable atmosphere has been found to have an ASL height ranging from 100–150 m, with the 500 m capping inversion height used in this study. It is important to note that the wind turbine’s hub height is 170 m, and all estimated ASL heights fall below this altitude. This highlights the wind turbine rotor’s exposure to the complex dynamics of the ABL at higher altitudes. These values appear consistent with the commonly accepted guideline that places the height of the atmospheric surface layer within the initial 10–20% of the atmospheric boundary layer (ABL) [33]. Based on the 500 m capping inversion in the present study, this guideline suggests the height of the atmospheric surface layer to be between 50–100 m.

The lateral and vertical co-coherence ( $\gamma_{uu}$ ) of the U component was analyzed. The focus was not on the longitudinal co-coherence or the other wind components, as previous research indicates that wind

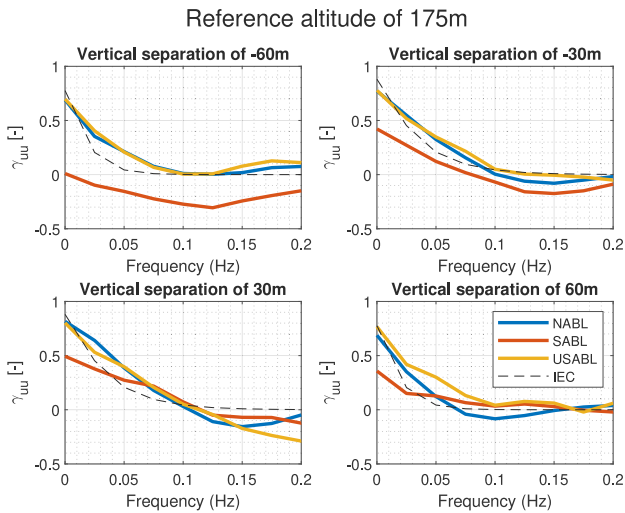
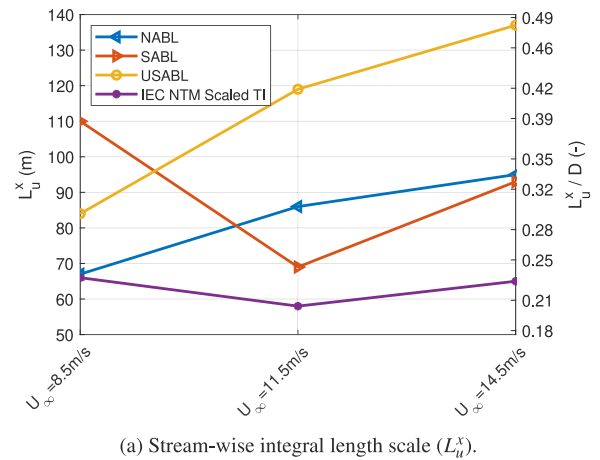


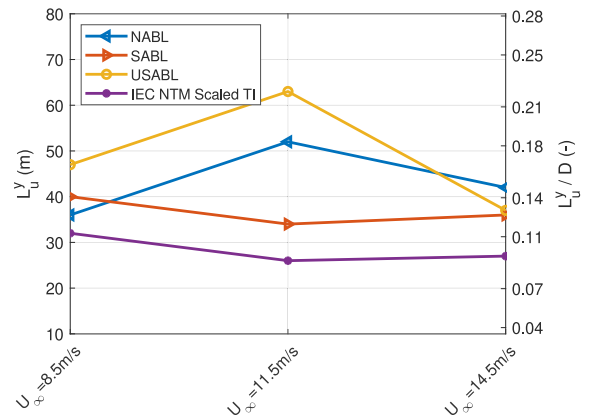
Fig. 7. Co-coherence for the U component at different vertical separations in the at-rated scenario. The measurement points are shown in Fig. 2.

turbine loads are most sensitive to the co-coherence of the stream-wise component in the lateral and vertical directions [68]. Four altitudes ranging from 125 m to 275 m were chosen in steps of 50 m along a base span location as shown in Fig. 2. The lateral co-coherence was then analyzed for points separated by 30 m, and 60 m. Further, the vertical co-coherence with a reference altitude was analyzed for vertical separations of  $\pm 30$  m and  $\pm 60$  m. Regarding the co-coherence, one common observation that can be made is that the IEC coherence function yields a sharp drop in the co-coherence at frequencies lower than 0.1 Hz, unlike the co-coherence observed in the LES wind fields, in the chosen laterally and vertical separations (Figs. 6 and 7). The vertical co-coherence is higher in the unstable and neutral atmosphere than in the stable atmosphere (Fig. 7). This result is intuitive considering the more shallow boundary layer in the stable atmospheres. The phase angle is disregarded in the IEC coherence function, but it can be seen that this is not the case with the LES wind fields and that co-coherence falls below zero on several occasions. However, the quad-coherence is not assessed because it is known to have negligible impact on the loads [67].

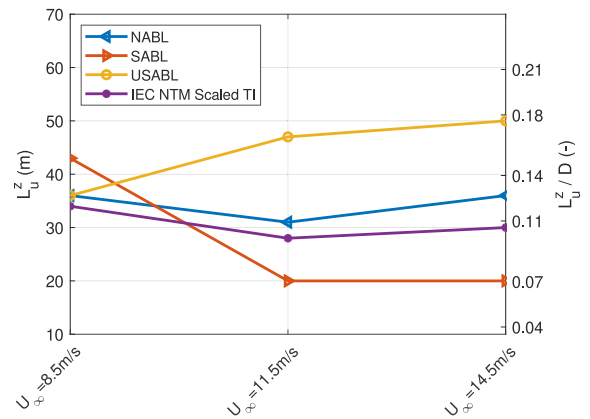
Lastly, the integral length scales shown in Fig. 8 represent the largest eddies in the ABL simulated in the present study. The estimates were computed using the approach shown in Eq. (11). The stream-wise ( $L_x^u$ ), span-wise ( $L_y^u$ ), and altitude-wise ( $L_z^u$ ) integral length scales are shown in Figs. 8(a), 8(b), and 8(c), respectively. The largest integral length scales are observed for the unstable atmosphere with  $L_x^u$  up to 0.5 times the rotor diameter, given the 500 m capping inversion used in this study. In contrast, it can be seen that the IEC Kaimal model cannot resolve large eddies and the variation of integral length scales with wind speeds. For instance, the largest  $L_x^u$  with the IEC Kaimal model wind fields is less than half of the integral length scales in the LES wind field with unstable atmosphere. It may be noted that the variation in the integral length scale across wind speeds intuitively complements the coherent structures visualized by SPOD. For instance, as shown in Fig. 8(a), the stream-wise integral length scale in an unstable atmosphere increases with wind speed. Similarly, a comparison between Figs. B.20 and B.24 reveals larger coherent structures in the latter case with higher wind speed. Interestingly, the integral length scales in the SABL are found to decrease with the wind speed (a similar trend also seen in [69]), which might be attributed to the energy content at lower frequencies at lower wind speeds. For example, the SPOD reveals that the 0.01 Hz mode has an energy of 26% (Fig. B.20(b)), 11% (Fig. 4(b)), and 21% (Fig. B.24(b)) for the below, at, and above-rated wind speeds.



(a) Stream-wise integral length scale ( $L_x^u$ ).



(b) Span-wise integral length scale ( $L_y^u$ ).



(c) Altitude-wise integral length scale ( $L_z^u$ ).

Fig. 8. Integral length scales of the U component at hub height, for the different wind fields. The left axis provides the absolute values and the right axis provides the values normalized with the rotor diameter.

#### 4.2. Impact of different coherent structures on loads

Based on the discussion in the previous section, it is evident that the LES wind fields in this study exhibit different characteristics compared to those generated by the IEC Kaimal model. Specifically, the LES wind fields feature larger integral length scales and more prominent coherent structures. Various frequency coherent structures were identified, and corresponding wind fields were reconstructed using SPOD.

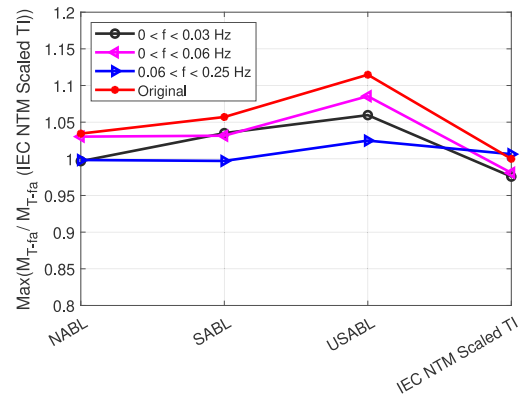
This section presents the aero-elastic analysis of the 22 MW RWT in these reconstructed wind fields. The analysis focuses on the tower base fore-aft bending moment ( $M_{T-fa}$ ), blade flap-wise bending moment ( $M_{flap}$ ), and azimuthal axial force contributing to thrust ( $F_x$ ). All values are normalized by the values corresponding to the scaled IEC Kaimal model-based original wind field. Here, originally refers to the initial wind field, that is, the wind field obtained from the respective method before SPOD and reconstruction.

Fig. 9 presents the  $max(M_{T-fa})$  in the different wind fields. In below-rated wind turbine operation (Fig. 9(a)), it can be seen that  $max(M_{T-fa})$  is consistently higher in the various LES wind fields, with the largest difference being approximately 10% in the unstable atmosphere. This trend correlates with the span-wise integral length scale ( $L_z^u$ ) shown in Fig. 8(b) for below-rated wind speed. At and above-rated wind turbine operation,  $max(M_{T-fa})$  is lower for the stable atmospheres, higher for the unstable atmosphere, and quite similar in the neutral atmosphere. This behavior in a stable atmosphere is attributed to the very low turbulence intensities, as seen in Figs. 3(b) and 3(c). Given the minor discrepancies ( $\pm 3\%$ ) observed between the neutral and scaled IEC Kaimal model-based wind fields at and above-rated wind turbine operation, it can be said that  $M_{T-fa}$  is insensitive to the coherent structures in these situations. A similar trend was observed for the mean values  $\overline{M_{T-fa}}$  (not shown here for brevity). Regarding the influence of different coherent structures, it is evident that much of the  $max(M_{T-fa})$  is captured by the lower frequency coherent structures, more so than by the higher frequency coherent structures. These structures have a larger amplitude and energy content. It has been consistently observed that wind fields with coherent structures at frequencies of  $\leq 0.06$  Hz can replicate much of the global response of a wind turbine. In contrast, wind fields with coherent structures in the 0.06–0.25 Hz range account for a smaller fraction of the wind turbine’s global response, suggesting that these structures primarily have a localized impact on the wind turbine.

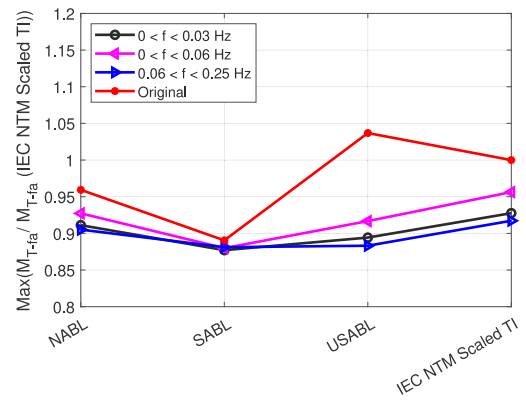
The comparison of  $max(M_{flap})$  is shown in Fig. 10. A similar trend is observed with smaller differences, than for  $max(M_{T-fa})$ . This lesser impact is expected because differences in  $M_{flap}$  tend to average out by the effects of shear and turbulence [69]. It is known that a higher wind shear leads to higher loads. Thus, the increased loads in the unstable atmosphere (low shear,  $\alpha \approx 0.04$ ) suggest the impact of the coherent structures.

Moreover, although the maximum design-driving loads discussed above show minimal differences between the neutral atmosphere and scaled IEC Kaimal model-based wind fields, a different observation was noted for the mean azimuthal blade loads. This is illustrated in Fig. 11. The mean axial force  $F_x$  differed by up to  $\pm 10\%$  (increase in the lower part and decrease in the upper part) in the neutral atmosphere, both below and above-rated operation, compared to the corresponding scaled IEC Kaimal model-based wind field. At-rated operation, this difference was up to  $\pm 5\%$  (increase in the lower part and decrease in the upper part). This smaller difference is attributed to the low turbulence intensity, which causes less variation in rotor thrust, resulting in consistently higher thrust compared to the scaled IEC Kaimal model-based wind field (as evident from the  $T_{f-a}$  comparison, which is dominated by rotor thrust). Given that the wind shear, turbulence intensity, and hub height wind speed are similar to the scaled IEC Kaimal model-based wind field, particularly in comparison to the neutral atmosphere, it can be concluded that the coherent structures and spatial flow characteristics cause the differences in azimuthal loads.

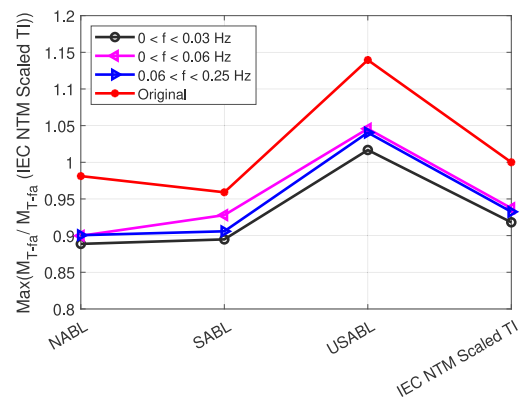
Next, the standard deviations of  $T_{f-a}$  and  $M_{flap}$  are presented in Figs. 12 and 13, respectively. From Fig. 12, it can be seen that  $\sigma_{T_{f-a}}$  is consistently higher (up to +50%) in the unstable atmosphere across all chosen wind turbine operating conditions. Conversely,  $\sigma_{T_{f-a}}$  is found to be lower (up to -50%) in the stable atmosphere, with an exception noted in Fig. 12(a). It is apparent from Fig. 8(c) that, for the case with a hub height wind speed of 8.5 m/s, the stable atmosphere has a higher altitude-wise integral length scale than the scaled IEC Kaimal wind



(a) Below Rated



(b) At Rated

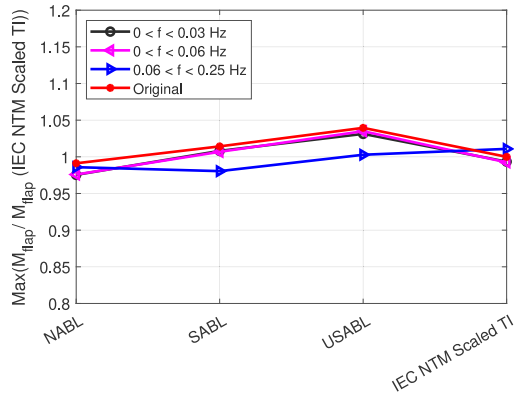


(c) Above Rated

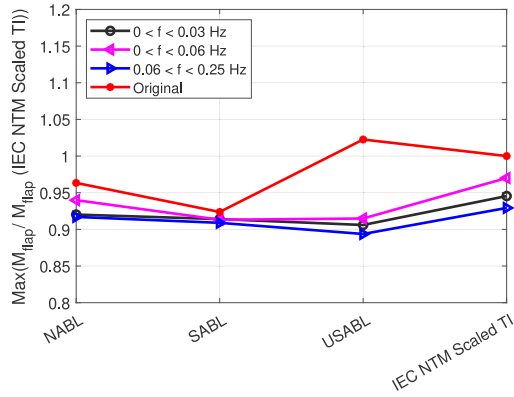
Fig. 9. Maximum values of tower fore-aft bending moment. Values are normalized with the corresponding values for the original IEC NTM Scaled TI scenario.

field. Therefore, considering the correlation of  $\sigma_{T_{f-a}}$  with  $L_z^u$ , it can be concluded that the larger eddies are responsible for the discrepancies observed.

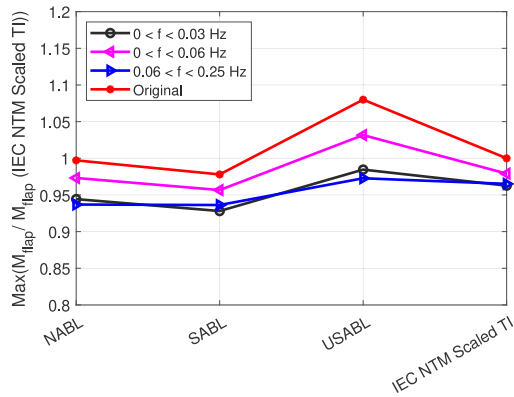
Fig. 13 shows that none of the LES wind fields lead to higher  $\sigma_{M_{flap}}$  compared to the scaled IEC Kaimal wind field. The only exception is the  $\sigma_{M_{flap}}$  in the stable atmosphere at above-rated operation (Fig. 13(c)). The neutral atmosphere wind fields result in similar  $\sigma_{M_{flap}}$  values, with an exception noted in Fig. 13(a). This exception is attributed to the higher energy content in the scaled IEC Kaimal wind field near the rotor’s 1P frequency, approximately 0.08 Hz. The SPOD results support this, showing that  $\sigma_{M_{flap}}$  is 75% lower in wind fields with



(a) Below Rated



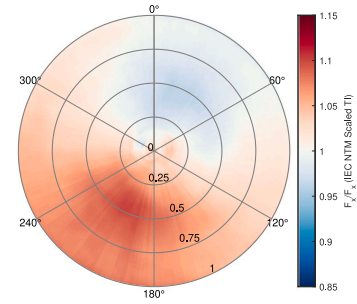
(b) At Rated



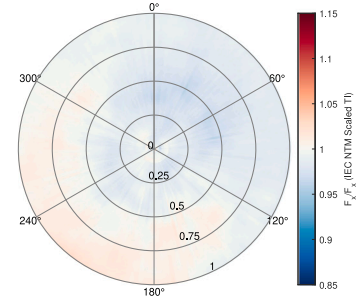
(c) Above Rated

Fig. 10. Maximum values of blade flap-wise bending moment. Values are normalized with the corresponding values for the original IEC NTM Scaled TI scenario.

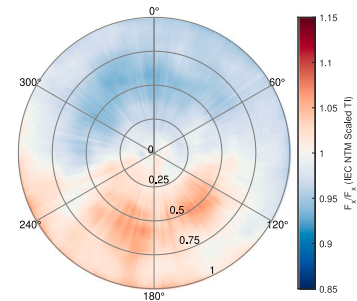
coherent structures between frequencies of 0.06 Hz and 0.25 Hz. The unstable atmosphere wind fields yield  $\sigma_{M_{flap}}$  values that are up to 25% lower. This decrease is attributed to the low wind shear in unstable atmospheres and relatively similar turbulence intensity, especially at higher altitudes (Fig. 3). Conversely, the stable atmosphere wind fields, despite their complex and high wind shear, lead to lower  $\sigma_{M_{flap}}$  values. This is due to the averaging effect of high wind shear combined with low turbulence intensity. These results align with the trends observed in [70].



(a) Below Rated



(b) At Rated



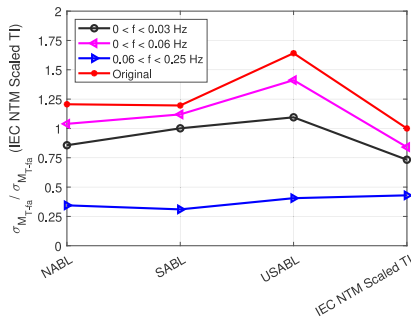
(c) Above Rated

Fig. 11. Azimuthal variation of axial force in NABL.

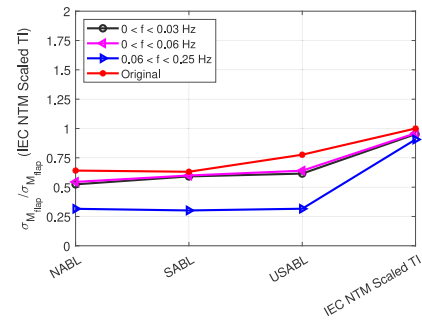
### 5. Conclusions and recommendations

The objective of this study was two-fold. Firstly, the objective was to assess how effectively the IEC Kaimal model represents the atmospheric inflow conditions at scales relevant to large wind turbines, specifically the IEA 22 MW wind turbine. Secondly, the study aimed to assess the aero-elastic response of the wind turbine under distinct inflow conditions characterized by varying atmospheric stability and wind speeds.

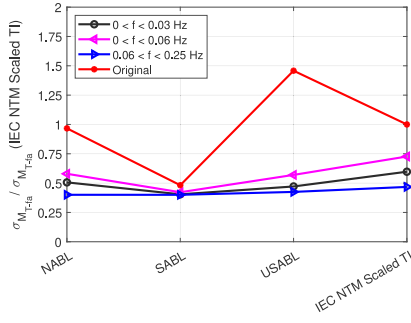
This study utilized low- and high-fidelity modeling. Wind fields based on the IEC Kaimal model were generated using NREL TurbSim, and LES with NREL SOWFA-6 simulated neutral, stable, and unstable conditions. The IEC fields were scaled to match the turbulence intensity and shear of LES neutral wind fields. Twelve wind fields were generated, decomposed, and reconstructed to capture coherent structures. Spectral Proper Orthogonal Decomposition (SPOD) was applied to isolate frequency-specific structures, with spectral analysis performed using co-coherence and integral length scale estimates. NREL OpenFAST was used to assess the wind turbine's aero-elastic response.



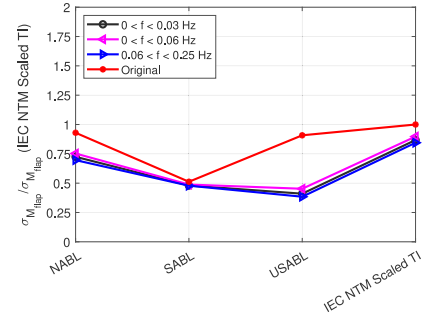
(a) Below Rated



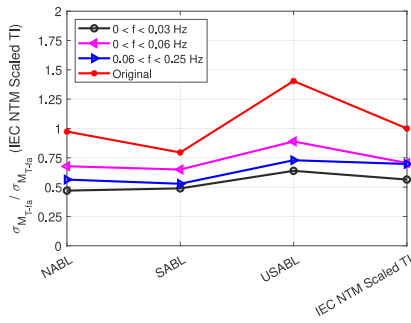
(a) Below Rated



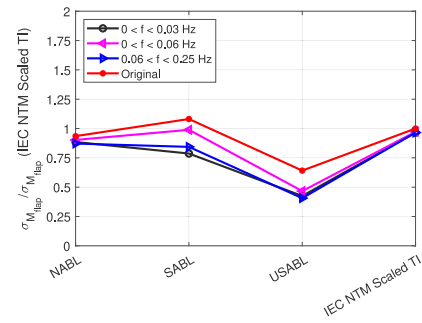
(b) At Rated



(b) At Rated



(c) Above Rated



(c) Above Rated

Fig. 12. Standard deviation of tower fore–aft bending moment. Values are normalized with the corresponding values for the original IEC NTM Scaled TI scenario.

Fig. 13. Standard deviation of blade flap-wise bending moment. Values are normalized with the corresponding values for the original IEC NTM Scaled TI scenario.

SPOD revealed the large coherent structures with low frequencies (0.01 Hz), which are horizontally stretched for the stable atmosphere while vertically stretched for the neutral and unstable atmosphere owing to the active vertical mixing. The IEC Kaimal model-based wind field were found to not contain these large coherent structures, especially in relation to the rotor diameter of 280m. Future work accompanying measurements at this scale will aid in gathering a more accurate estimate of the coherent structures. The SPOD results were complemented through integral length scale estimates. With the 500 m capping inversion used in this study, it was found that the LES wind fields exhibited stream-wise integral length scales sized 70–140 m or 0.2–0.5D (highest for the unstable atmosphere in the above-rated wind speed scenario) while the IEC Kaimal model-based wind field had  $L_u^x$  of 0.2D. Additionally, the IEC Kaimal model did not capture the variation of  $L_u$  with wind speeds.

Regarding wind field co-coherence, discrepancies between LES and IEC Kaimal model-based wind fields were pronounced, especially at higher altitudes. In LES-based wind fields, coherent structures decayed less rapidly at lower frequencies, highlighting their larger size than the IEC Kaimal model. Stable atmospheres exhibited lower vertical

co-coherence, while neutral atmospheres generally showed higher co-coherence at frequencies of interest ( $\leq 0.2$  Hz). A friction velocity-based ASL height estimate revealed that the ASL height varied from 100 to 150 m depending on stratification, with a notable case of a shallow stable atmosphere resulting in an ASL height of 25 m. Hence, the IEA 22 MW wind turbine, with a maximum tip height of approximately 310 m, has most of its rotor exposed to complex ABL dynamics that exceed the modeling capabilities of the IEC Kaimal model-based wind fields.

The aero-elastic response was evaluated using BEM on NREL OpenFAST. The analysis was focused on tower fore–aft bending moment ( $T_{f-a}$ ), blade root flap-wise bending moment ( $M_{flap}$ ), and axial force ( $F_x$ ) contributing to thrust. It was found that the design driving  $max(T_{f-a})$  and  $max(M_{flap})$  are higher by up to 15% and up to 8% respectively, in comparison to the scaled IEC Kaimal model-based wind field. The azimuthal variation of  $F_x$  revealed differences (up to  $\pm 7.5\%$ ) along the rotor for even the case of a neutral atmosphere compared to the scaled IEC Kaimal model-based wind field. These discrepancies were attributed to the coherent structures given the similar wind shear and turbulence intensity. The discrepancies were larger for the

below and above-rated operating conditions than for rated operating conditions. The variation of  $\sigma(T_{f-a})$  showed differences up to +50% for unstable atmosphere, compared to the IEC NTM Scaled TI wind field, at all operating conditions. In contrast, the difference was -50% for stable atmospheres. The variation of  $T_{f-a}$  was found to correlate with  $L_u^z$ . The parameter  $\sigma(M_{flap})$  was found to be less sensitive to the atmospheric stratification with a maximum change of -25%. The contrasting effect of high (low) wind shear and low (high) turbulence intensity was attributed to the observed variation. Much of the observed variation was captured by the low frequency ( $\leq 0.06$  Hz) SPOD modes.

In conclusion, IEC Kaimal model must incorporate the ability to represent coherent structures indicative of the desired atmospheric stratification. The higher coherence observed at higher altitudes, above the ASL, underscores the need to develop more comprehensive coherence models. This will be the next step in the research, likely requiring validation with measurements at these higher altitudes. Further examining the relationships between integral length scales and lateral and vertical coherence could help refine current models. This will help enhance the current formulation of the IEC Kaimal model coherence which has same decay in lateral and vertical directions. Furthermore, analyzing the reconstructed SPOD wind fields could provide insights into low-frequency coherent structures, aiding model development. Regarding the aero-elastic response, the next step will be to assess the loads using higher-fidelity modeling.

**CRedit authorship contribution statement**

**Nirav Dangı:** Writing – original draft, Methodology, Investigation, Formal analysis, Data curation, Conceptualization. **Jurij Sodja:** Writing – review & editing, Supervision. **Carlos Simão Ferreira:** Writing – review & editing, Supervision, Project administration, Funding acquisition. **Wei Yu:** Writing – review & editing, Supervision, Project administration, Funding acquisition.

**Declaration of competing interest**

The authors declare that they have no known competing financial interests or personal relationships that could have appeared to influence the work reported in this paper.

**Acknowledgments**

This research was supported by the Korea Institute of Energy Technology Evaluation and Planning(KETEP) grant funded by the Korea Government (MOTIE) (20228520020050).

The authors thank the Delft High Performance Computing Centre (<https://www.tudelft.nl/dhpc>) for the use of computational resources of the DelftBlue supercomputer.

The authors thank SURF ([www.surf.nl](http://www.surf.nl)) for the support in using the Dutch National Supercomputer Snellius.

**Appendix A. Wind field characteristics**

Fig. A.14 provides the wind field energy spectrum for the justification of the chosen cut-off frequency of 0.25 Hz.

Next, an example visualization of the wind field characteristics of the decomposed (Fig. A.15) and reconstructed wind fields (Figs. A.16 and A.17) by utilizing SPOD is shown below.

The calculated friction velocity and estimated ASL height (in line with approach in Section 2.3) are shown in Fig. A.18.

Fig. A.19 below shows the wind turbine induction zone wind speed profile to justify the choice of 3D upstream distance for sampling free-stream wind field.

**Appendix B. Wind field decomposition and spectral analysis**

See Figs. B.20–B.27, in addition to results provided in Section 4.1.

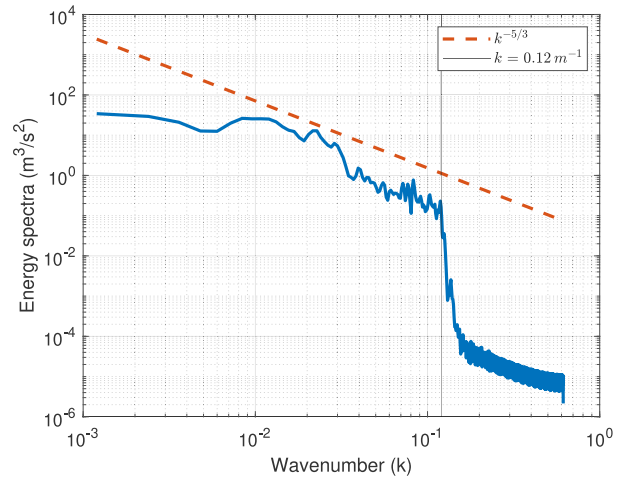


Fig. A.14. Example visualization of wind field spectrum for the at-rated wind speed scenario in a stable atmosphere. The cut-off frequency was identified as the one corresponding to the highest wavenumber (denoted as black line) in the inertial subrange of the LES.

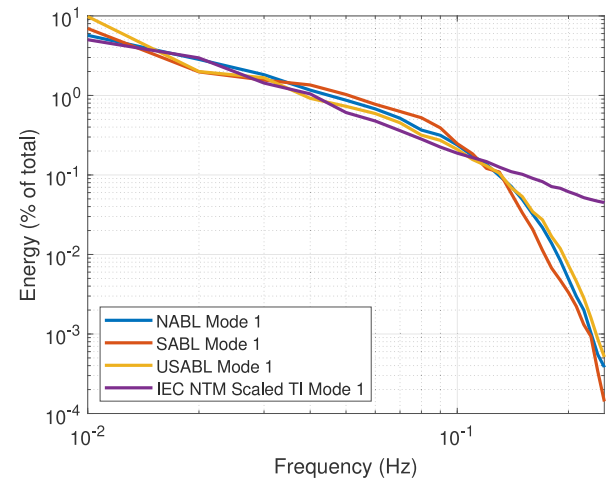


Fig. A.15. Energy distribution of the leading SPOD mode across different frequencies. The SPOD identified 13 modes for each frequency.

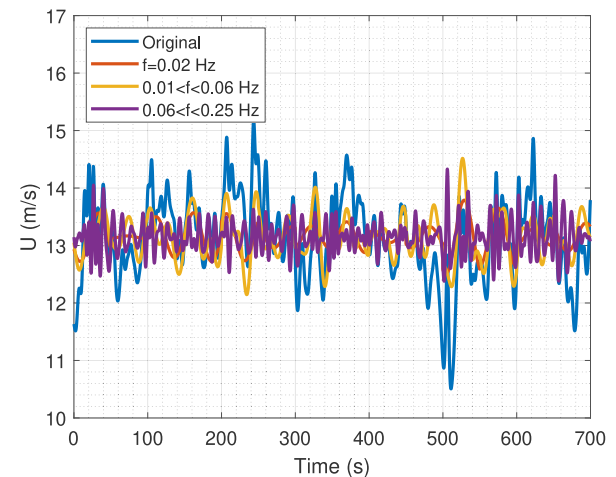


Fig. A.16. Instantaneous U component with different frequencies, compared to the original wind field. All modes at the corresponding frequency were used to reconstruct the velocity.

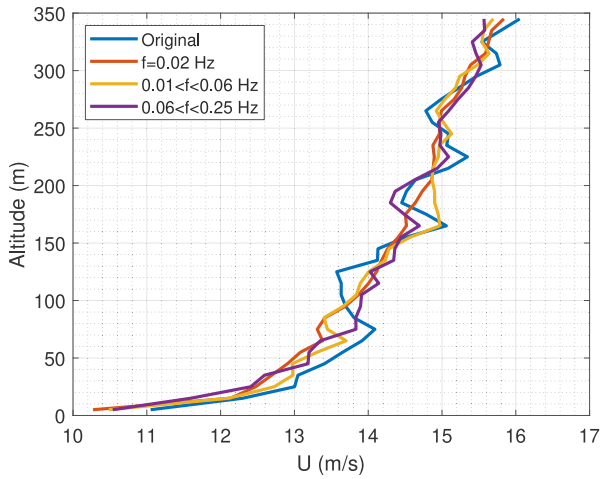


Fig. A.17. Example visualization of the results of the spectral orthogonal decomposition (SPOD).

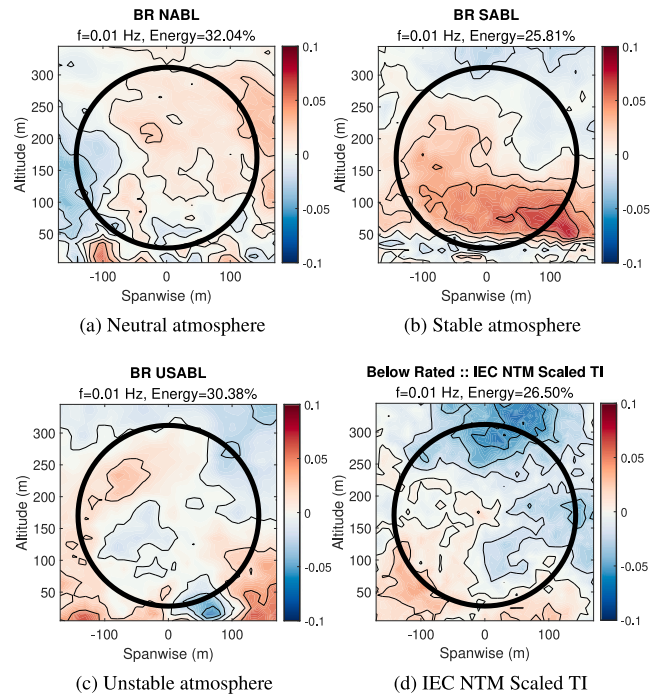


Fig. B.20. SPOD mode 1 with frequency 0.01 Hz in the below-rated scenario.

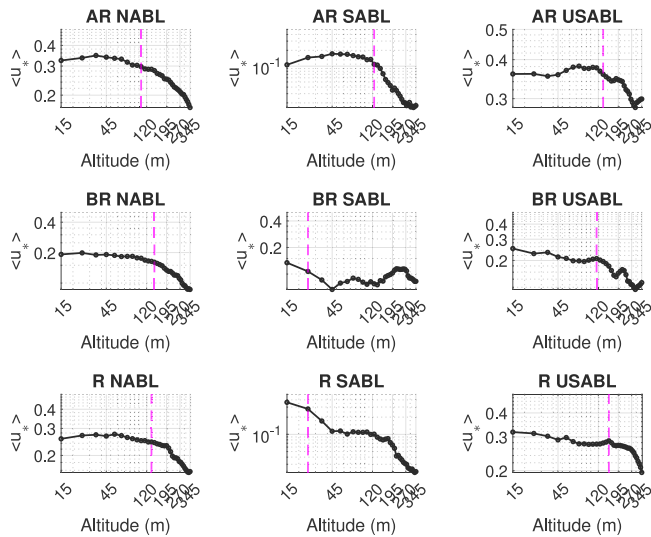


Fig. A.18. Friction velocity in different inflow conditions plotted against the altitude. The magenta lines indicate the estimated atmospheric surface layer height.

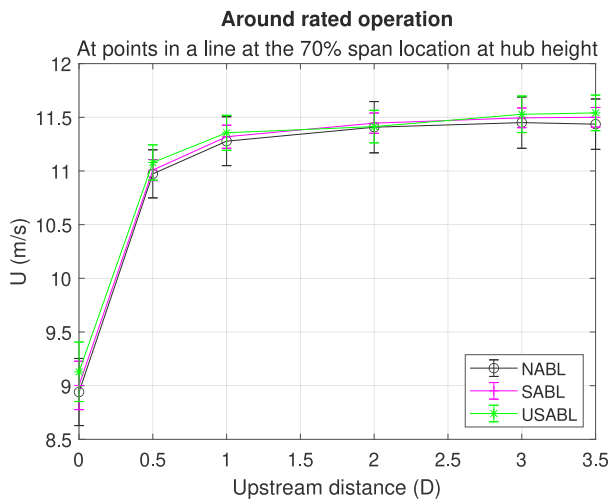


Fig. A.19. Wind turbine upstream region wind profile to show the negligible influence of induction zone at 3D upstream distance.

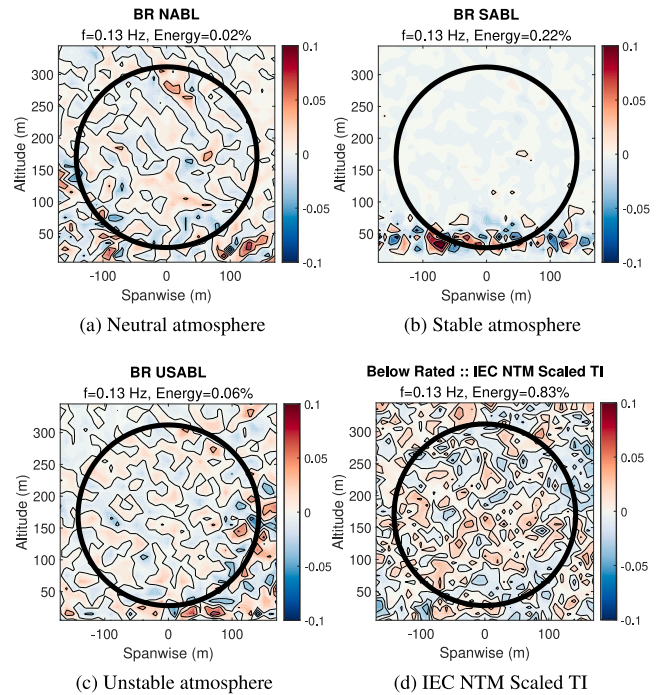
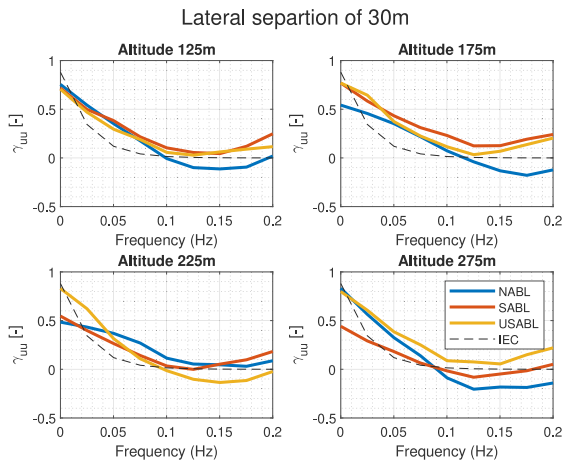


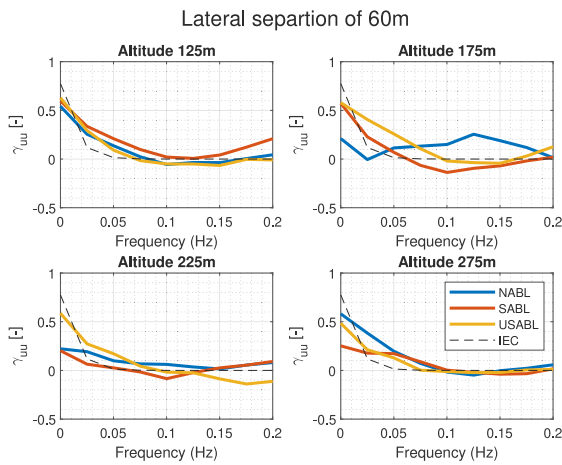
Fig. B.21. SPOD mode 1 with frequency 0.13 Hz in the below-rated scenario.

### Appendix C. Spectral proper orthogonal decomposition validation

The current implementation of the SPOD, as outlined in [43], was validated using a simulation dataset of the von Kármán vortex street, which was extracted from [71,72]. The authors conducted a 2D Unsteady Cylinder Flow in a simulation domain spanning from  $-0.5$  m to  $7.5$  m in the stream-wise direction and  $-0.5$  m to  $0.5$  m in the span-wise direction. Their simulation was conducted at a Reynolds number (Re) of 160 and a cylinder of radius  $0.0625$  m was placed at the origin



(a) Lateral separation of 30m.



(b) Lateral separation of 60m.

Fig. B.22. Co-coherence for the U component at different lateral separations and altitudes in the below-rated scenario. The measurement points are shown in Fig. 2.

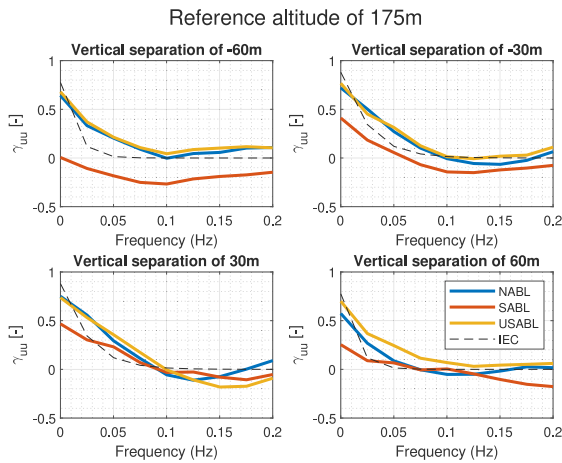


Fig. B.23. Co-coherence for the U component at different vertical separations in the below-rated scenario. The measurement points are shown in Fig. 2.

of the domain (0m, 0m). An example visualization of the flow is shown in Fig. C.28 and the time-averaged flow field is shown in Fig. C.29.

This case was chosen because one can estimate the vortex shedding frequency of the swirling vortices in the von Kármán vortex street. This

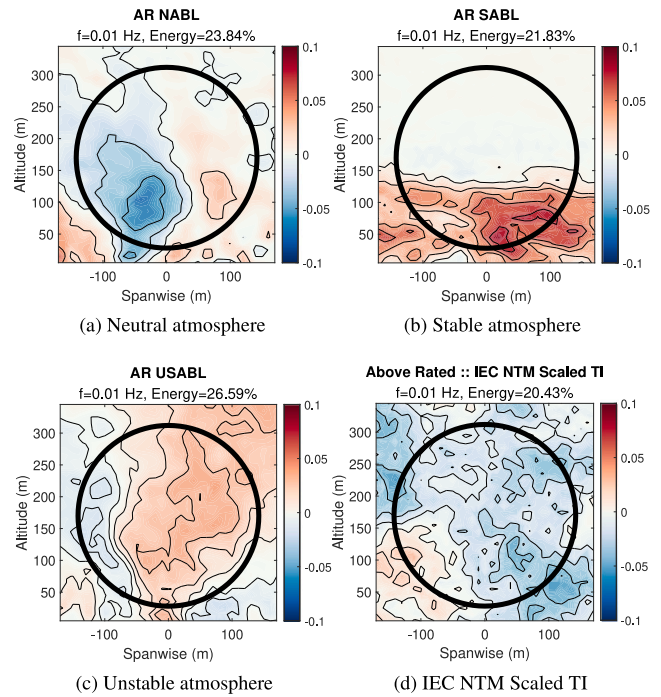


Fig. B.24. SPOD mode 1 with frequency 0.01 Hz in the above-rated scenario.

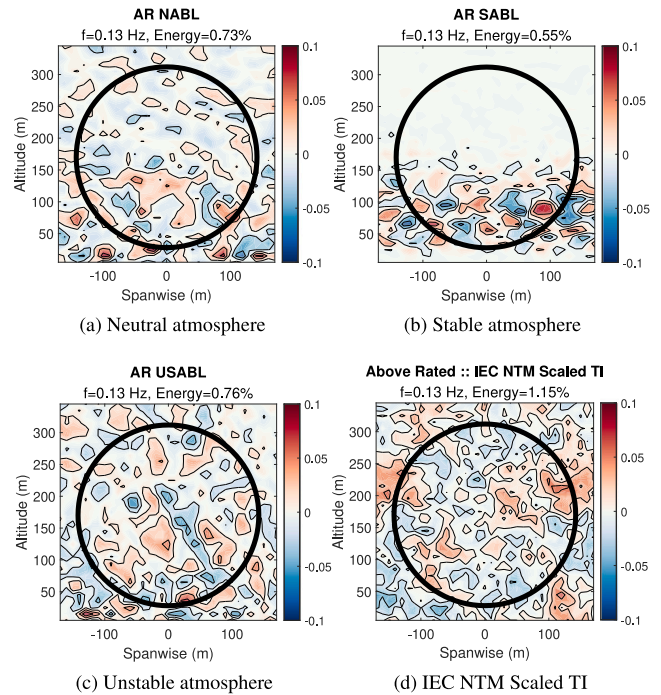


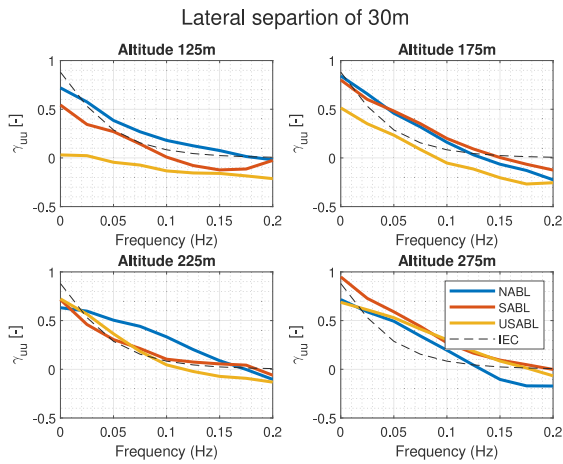
Fig. B.25. SPOD mode 1 with frequency 0.13 Hz in the above-rated scenario.

can be done by using Eq. (C.1) [73] and Eq. (C.2).

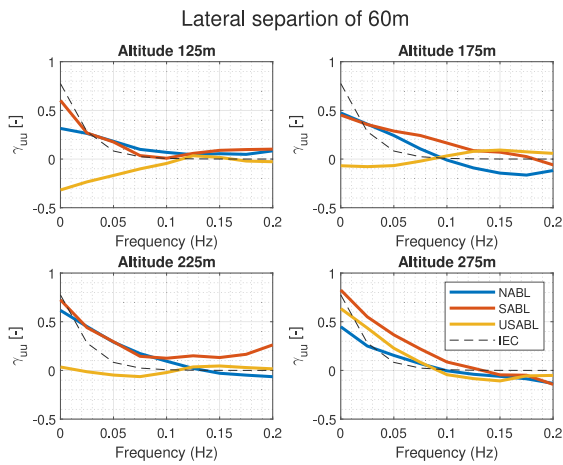
$$St = 0.2655 - \frac{1.018}{\sqrt{Re}} \quad (C.1)$$

$$f = \frac{U * St}{d} \quad (C.2)$$

In the above equations,  $St$  is the dimensionless Strouhal number,  $f$  is the vortex shedding frequency,  $U$  is the flow velocity in m/s and  $d$  is the length scale of the body, here the cylinder diameter. Plugging in



(a) Lateral separation of 30m.



(b) Lateral separation of 60m.

Fig. B.26. Co-coherence for the U component at different lateral separations and altitudes in the above-rated scenario. The measurement points are shown in Fig. 2.

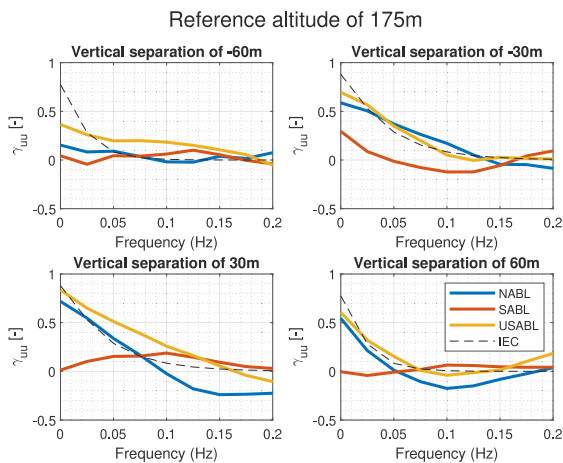


Fig. B.27. Co-coherence for the U component at different vertical separations in the above-rated scenario. The measurement points are shown in Fig. 2.

the values in the above equation, it can be found that  $f$  is  $\approx 1.5$  Hz.

The SPOD procedure described in Section 2.2 was utilized on the above data-set. Fig. C.30 presents the SPOD modes of the flow at distinct frequencies. Based on the above calculation, it was expected

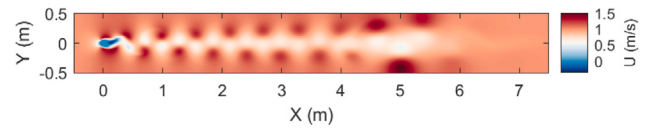


Fig. C.28. An instantaneous visualization of the flow-field of the 2-D unsteady flow simulation extracted from [71,72].

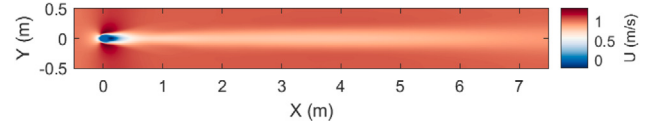


Fig. C.29. A visualization of the time-averaged flow-field of the 2-D unsteady flow simulation extracted from [71,72].

that the vortex shedding would be observed at  $\approx 1.5$  Hz and in its integer multiples, albeit with lower energy. Figs. C.30(c) to C.30(f) illustrate this expectation and the lower frequencies show large structures not related to the von Kármán vortex street.

#### Appendix D. Sensitivity study of large eddy simulations of the stable atmospheric boundary layer

A sensitivity study of the LES of the stable atmosphere was conducted to determine whether under-resolved small-scale structures on a coarser grid affect the wind turbine loads. The results presented in this section are meant to highlight aspects relevant to this study rather than provide an in-depth analysis of the differences. For a detailed understanding of the sensitivity of ABL-LES results, the reader is referred to [53] and the references therein.

To keep the computational cost reasonable this study was conducted on a domain smaller than the one utilized (Fig. 1) in the main study. Three domains with size  $640\text{ m} \times 640\text{ m} \times 640\text{ m}$  were utilized with isotropic grids of size 10m, 5m and 3.125m (in line with [74]). The solver settings were identical to those detailed in Section 3, except that the inversion layer height was set to 200m in the cases of this sensitivity study.

From Fig. D.31 it can be seen that an acceptable quasi-steady state has been achieved. Similar checks were made on the temperature, surface flux, boundary layer height (not shown here for brevity). From the planar-averaged velocity profile in Fig. D.32, it can be seen that the boundary layer becomes shallower, that is, for example, the maximum velocity is reached at a lower altitude as the grid is refined. The fluctuations in the lower altitudes are found to be resolved better with the finer grid while the mean velocity profile has no remarkable differences, apart from a slight offset in wind speed at heights about the inversion layer. This offset was found to be linked to a slightly different strength of the inertial oscillations in the coarse LES than in the fine resolution LES (also see section 2 and 3.4 of [75]). The change in wind speed profiles due to this effect will manifest only above the boundary layer and are not expected to affect the wind profiles in the rotor exposed area in the main study, which used a higher inversion height.

Upon plotting the spectra of the wind field (not shown here), as expected, there was an increase in energy at higher frequencies. However, a drop in energy spectrum was found at very low frequencies. In a recent paper [75], this behavior has been observed too, but their study could not provide a reasonable explanation for this behavior (see section 3.4.6 of their study). The author of [76] finds high SGS model dissipation at small wave-numbers and hypothesizes it to be linked to the effective filter width. Figure 7 of [53] also shows this trend, however, their study does not discuss it. Owing to these discrepancies and open-questions, these stable ABL-LES wind fields were

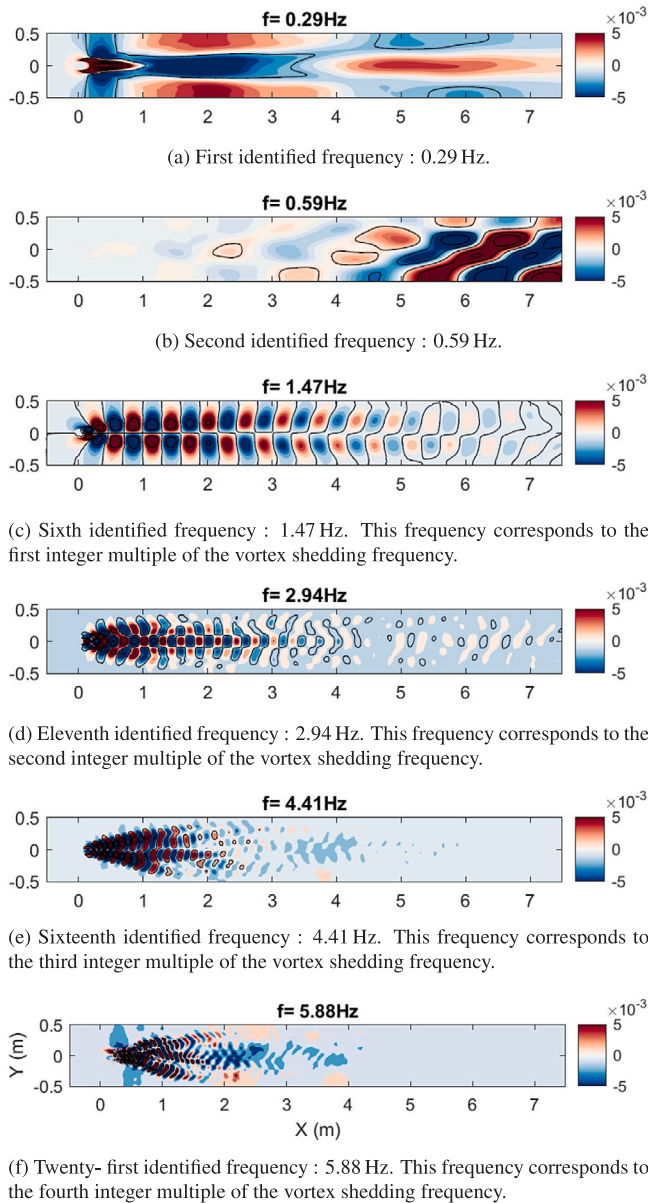


Fig. C.30. SPOD mode 1 for different frequencies in the 2-D unsteady flow simulation extracted from [71,72].

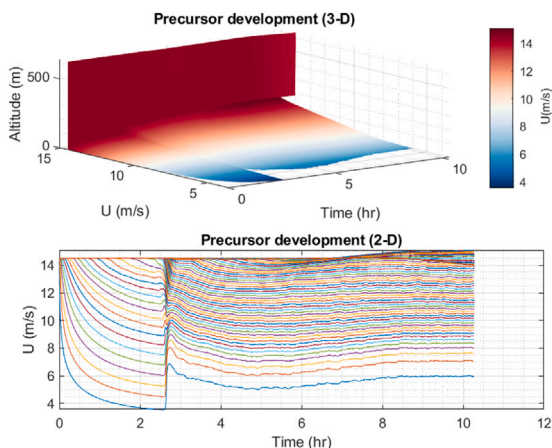


Fig. D.31. Visualization of the development of the stable atmosphere precursor with isotropic grid size of 3.125 m.

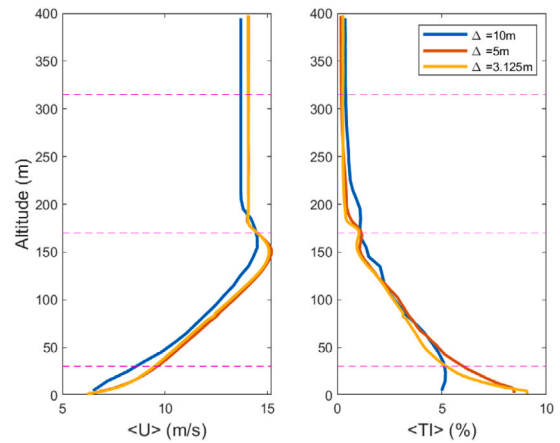


Fig. D.32. Spatio-temporal averaged profiles for the stable atmosphere precursors with three different grid sizes. The averaging was conducted over the last 1000 s of the precursor. The magenta lines indicate the rotor tips and hub height.

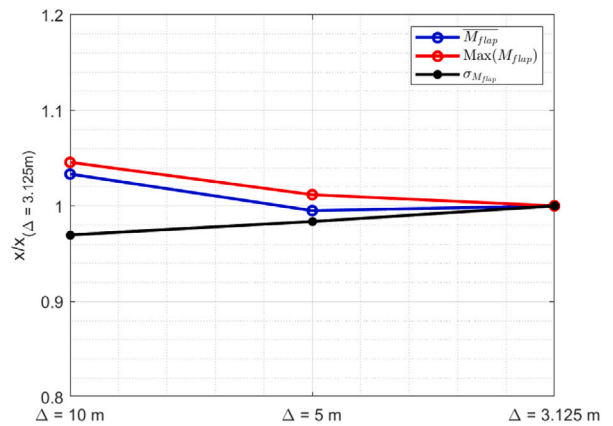


Fig. D.33. Blade flap-wise bending moment variation due to LES grid size.

input to standalone OpenFAST simulations as in the main study and the aero-elastic impact was assessed on the IEA 22 MW wind turbine. The blade flap-wise bending moment and tower fore-aft bending moment are known to be sensitive to low-frequency wind fluctuations. Hence, a slight increase (+4%) in maximum value of blade-flap-wise ( $\max(M_{\text{flap}})$ ) bending moment was found, for the coarser LES simulation (Fig. D.33). Given the lower energy of high-frequency fluctuations in the coarser simulation, the standard deviation ( $\sigma_{M_{\text{flap}}}$ ) has been found to be marginally lower (-3%). A similar trend was seen for the tower fore-aft bending moment. With this observation, it can be noted that there is no major necessity for the use of the finer grid for the purpose of this study, which revolves around large-scale structures.

References

- [1] International Electrotechnical Commission (IEC), IEC 61400-1:2019, 2019, URL <https://webstore.iec.ch/publication/26423>.
- [2] Paul Veers, Carlo L. Bottasso, Lance Manuel, Jonathan Naughton, Lucy Pao, Joshua Paquette, Amy Robertson, Michael Robinson, Shreyas Ananthan, Thanasis Barlas, Alessandro Bianchini, Henrik Bredmose, Sergio González Horcas, Jonathan Keller, Helge Aagaard Madsen, James Manwell, Patrick Moriarty, Stephen Nolet, Jennifer Rinker, Grand challenges in the design, manufacture, and operation of future wind turbine systems, Wind Energy Sci. (ISSN: 23667451) 8 (7) (2023) 1071–1131, <http://dx.doi.org/10.5194/WES-8-1071-2023>.
- [3] J. Mann, The spatial structure of neutral atmospheric surface-layer turbulence, J. Fluid Mech. (ISSN: 0022-1120) 273 (1994) 141–168, URL <https://orbit.dtu.dk/en/publications/the-spatial-structure-of-neutral-atmospheric-surface-layer-turbul>.

- [4] J.C. Kaimal, J.C. Wyngaard, Y. Izumi, O.R. Coté, Spectral characteristics of surface-layer turbulence, *Q. J. R. Meteorol. Soc.* (ISSN: 1477-870X) 98 (417) (1972) 563–589, <http://dx.doi.org/10.1002/QJ.49709841707>, URL <https://onlinelibrary.wiley.com/doi/full/10.1002/qj.49709841707>.
- [5] Robert Thresher, W.E. Holley, C.E. Smith, N. Jafarey, S.R. Lin, *Modeling the response of wind turbines to atmospheric turbulence*, 1981.
- [6] A.G. Davenport, The application of statistical concepts to the wind loading of structures, *Proc. Inst. Civ. Eng.* 19 (4) (1961) 449–472, <http://dx.doi.org/10.1680/iicep.1961.11304>.
- [7] Liang Dong, Wai Hou Lio, Eric Simley, On turbulence models and lidar measurements for wind turbine control, *Wind Energy Sci.* (ISSN: 23667451) 6 (6) (2021) 1491–1500, <http://dx.doi.org/10.5194/WES-6-1491-2021>.
- [8] A.G. Davenport, The response of slender, line-like structures to a gusty wind. 23.3, pp. 389–408. <http://dx.doi.org/10.1680/IICEP.1962.10876>. URL <https://www.icevirtuallibrary.com/doi/10.1680/iicep.1962.10876>.
- [9] Rick Soucy, Robert Woodward, H.A. Panofsky, Vertical cross-spectra of horizontal velocity components at the boulder observatory, *Bound.-Layer Meteorol.* (ISSN: 00068314) 24 (1) (1982) 57–66, <http://dx.doi.org/10.1007/BF00121799/METRICS>, URL <https://link.springer.com/article/10.1007/BF00121799>.
- [10] C. Sacré, D. Delaunay, Structure spatiale de la turbulence au cours de vents forts sur différents sites, *J. Wind Eng. Ind. Aerodyn.* (ISSN: 0167-6105) 41 (1–3) (1992) 295–303, [http://dx.doi.org/10.1016/0167-6105\(92\)90424-9](http://dx.doi.org/10.1016/0167-6105(92)90424-9).
- [11] Rieska Mawarni Putri, Etienne Cheynet, Charlotte Ohrai, Jasna Bogunovic Jakobsen, Turbulence in a coastal environment: the case of vindeby, *Wind Energy Sci.* (ISSN: 23667451) 7 (4) (2022) 1693–1710, <http://dx.doi.org/10.5194/WES-7-1693-2022>.
- [12] Lene Eliassen, Søren Andersen, Investigating coherent structures in the standard turbulence models using proper orthogonal decomposition, *J. Phys. Conf. Ser.* 753 (3) (2016) 32040, <http://dx.doi.org/10.1088/1742-6596/753/3/032040>.
- [13] A.K.M.F. Hussain, Coherent structures—reality and myth, *Phys. Fluids* (ISSN: 0031-9171) 26 (10) (1983) 2816–2850, <http://dx.doi.org/10.1063/1.864048>, URL <http://aip/pfi/article/26/10/2816/943732/Coherent-structures-reality-and-myth>.
- [14] Astrid Nybø, Finn Gunnar Nielsen, Joachim Reuder, Matthew J. Churchfield, Marte Godvik, Evaluation of different wind fields for the investigation of the dynamic response of offshore wind turbines, *Wind Energy* (ISSN: 1099-1824) 23 (9) (2020) 1810–1830, <http://dx.doi.org/10.1002/WE.2518>, URL <https://onlinelibrary.wiley.com/doi/full/10.1002/we.2518>.
- [15] A. Nybø, F.G. Nielsen, M. Godvik, Analysis of turbulence models fitted to site, and their impact on the response of a bottom-fixed wind turbine, *J. Phys. Conf. Ser.* 2018 (1) (2021) 12028, <http://dx.doi.org/10.1088/1742-6596/2018/1/012028>.
- [16] M.C. Holtslag, W.A.A.M. Bierbooms, G.J.W. van Bussel, Wind turbine fatigue loads as a function of atmospheric conditions offshore, *Wind Energy* (ISSN: 1099-1824) 19 (10) (2016) 1917–1932, <http://dx.doi.org/10.1002/WE.1959>, URL <https://onlinelibrary.wiley.com/doi/full/10.1002/we.1959>.
- [17] Paula Doubrawa, Matthew J. Churchfield, Marte Godvik, Senu Sirmivas, Load response of a floating wind turbine to turbulent atmospheric flow, *Appl. Energy* (ISSN: 0306-2619) 242 (2019) 1588–1599, <http://dx.doi.org/10.1016/J.APENERGY.2019.01.165>.
- [18] Erin E. Bachynski, Lene Eliassen, The effects of coherent structures on the global response of floating offshore wind turbines, *Wind Energy* (ISSN: 1099-1824) 22 (2) (2019) 219–238, <http://dx.doi.org/10.1002/WE.2280>, URL <https://onlinelibrary.wiley.com/doi/full/10.1002/we.2280>.
- [19] Yan Wang, Ronghu Guan, Liang Wang, Pan Lu, Influence of turbulent coherent structures on the performance and wake of a wind turbine, *Eur. J. Mech. B Fluids* (ISSN: 0997-7546) 105 (2024) 104–118, <http://dx.doi.org/10.1016/J.EUROMECHFLU.2024.01.002>.
- [20] Kunihiko Taira, Steven L Brunton, Scott T M Dawson, Clarence W Rowley, Tim Colonius, Beverley J McKeon, Oliver T Schmidt, Stanislav Gordeyev, Vassilios Theofilis, Lawrence S Ukeiley, Modal analysis of fluid flows: An overview, *AIAA J.* 55 (12) (2017) 4013–4041, <http://dx.doi.org/10.2514/1.J056060>.
- [21] Brooke J. Stanislawski, Regis Thedin, Ashesh Sharma, Emmanuel Branlard, Ganesh Vijayakumar, Michael A. Sprague, Effect of the integral length scales of turbulent inflows on wind turbine loads, *Renew. Energy* (ISSN: 0960-1481) 217 (2023) 119218, <http://dx.doi.org/10.1016/J.RENENE.2023.119218>.
- [22] N.S. Dangi, W. Yu, J. Sodja, C.S. Ferreira, Aeroelastic analysis of a very large wind turbine in various atmospheric stability conditions, *J. Phys. Conf. Ser.* (ISSN: 1742-6596) 2767 (5) (2024) 052026, <http://dx.doi.org/10.1088/1742-6596/2767/5/052026>.
- [23] R.J. Barthelmie, The effects of atmospheric stability on coastal wind climates, *Meteorol. Appl.* 6 (1) (1999) 39–47, <http://dx.doi.org/10.1017/S1350482799000961>, URL <https://rmts.onlinelibrary.wiley.com/doi/abs/10.1017/S1350482799000961>.
- [24] Ameya Sathe, Sven-Erik Gryning, Alfredo Peña, Comparison of the atmospheric stability and wind profiles at two wind farm sites over a long marine fetch in the North Sea, *Wind Energy* 14 (6) (2011) 767–780, <http://dx.doi.org/10.1002/we.456>, URL <https://onlinelibrary.wiley.com/doi/abs/10.1002/we.456>.
- [25] Etienne Cheynet, Jasna B. Jakobsen, Joachim Reuder, Velocity spectra and coherence estimates in the marine atmospheric boundary layer, *Bound.-Layer Meteorol.* (ISSN: 15731472) 169 (3) (2018) 429–460, <http://dx.doi.org/10.1007/S10546-018-0382-2/TABLES/3>, URL <https://link.springer.com/article/10.1007/s10546-018-0382-2>.
- [26] Leonardo Alcayaga, Gunner Chr Larsen, Mark Kelly, Jakob Mann, Identification of large-scale atmospheric structures under different stability conditions using dynamic mode decomposition, *J. Phys. Conf. Ser.* (ISSN: 17426596) 2265 (2) (2022) 022006, <http://dx.doi.org/10.1088/1742-6596/2265/2/022006>, URL <https://orbit.dtu.dk/en/publications/identification-of-large-scale-atmospheric-structures-under-differ>.
- [27] IEA Wind Task 37, IEAWindTask37/IEA-22-280-RWT, 2023, URL <https://github.com/IEAWindTask37/IEA-22-280-RWT>.
- [28] Frederik Zahle, Thanasis Barlas, Kenneth Lønæk, Pietro Bortolotti, Daniel Zalkind, Lu Wang, Casper Labuschagne, Latha Sethuraman, Garrett Barter, Definition of the IEA wind 22-megawatt offshore reference wind turbine, 2024, <http://dx.doi.org/10.11581/DTU.00000317>, URL <https://backend.orbit.dtu.dk/ws/files/357327260/iea-22-280-rwt-report.pdf>.
- [29] Matthew Churchfield, Sang Lee, Patrick Moriarty, Overview of the simulator for wind farm application (SOWFA), 2012, URL <http://wind.nrel.gov/designcodes/simulators/sowfa/>.
- [30] H.G. Weller, G. Tabor, H. Jasak, C. Fureby, A tensorial approach to computational continuum mechanics using object-oriented techniques, *Comput. Phys.* (ISSN: 0894-1866) 12 (6) (1998) 620–631, <http://dx.doi.org/10.1063/1.168744>, URL <http://dx.doi.org/10.1063/1.168744>.
- [31] B.J. Jonkman, *TurbSim User's Guide*, Tech. rep., National Renewable Energy Laboratory (NREL), 2014, URL [www.nrel.gov/publications](http://www.nrel.gov/publications).
- [32] Jason Jonkman, Mike Sprague, et al., OpenFAST | Wind Research | NREL, 2022, URL <https://www.nrel.gov/wind/nwtc/openfast.html>.
- [33] Roland Stull, *Practical meteorology: An algebra-based survey of atmospheric science*, 2017, URL [https://www.eoas.ubc.ca/books/Practical\\_Meteorology/](https://www.eoas.ubc.ca/books/Practical_Meteorology/).
- [34] Matthew J. Churchfield, Sang Lee, John Michalakes, Patrick J. Moriarty, A numerical study of the effects of atmospheric and wake turbulence on wind turbine dynamics, *J. Turbul.* (ISSN: 14685248) 13 (2012) 1–32, <http://dx.doi.org/10.1080/14685248.2012.668191>, URL <https://www.tandfonline.com/doi/abs/10.1080/14685248.2012.668191>.
- [35] Srinidhi N. Gadde, Richard J.A.M. Stevens, Effect of low-level jet height on wind farm performance, *J. Renew. Sustain. Energy* (ISSN: 19417012) 13 (1) (2021) 13305, <http://dx.doi.org/10.1063/5.0026232/284849>, URL <http://dx.doi.org/10.1063/5.0026232/284849>.
- [36] Chin-Hoh Moeng, A large-eddy-simulation model for the study of planetary boundary-layer turbulence, *J. Atmos. Sci.* 41 (13) (1984) 2052–2062, [http://dx.doi.org/10.1175/1520-0469\(1984\)041<2052:ALESMP>2.0.CO;2](http://dx.doi.org/10.1175/1520-0469(1984)041<2052:ALESMP>2.0.CO;2), URL [https://journals.ametsoc.org/view/journals/atsc/41/13/1520-0469\\_1984\\_041\\_2052\\_alesmf\\_2\\_0\\_co\\_2.xml](https://journals.ametsoc.org/view/journals/atsc/41/13/1520-0469_1984_041_2052_alesmf_2_0_co_2.xml).
- [37] James W. Deardorff, Stratocumulus-capped mixed layers derived from a three-dimensional model, *Bound.-Layer Meteorol.* (ISSN: 1573-1472) 18 (4) (1980) 495–527, <http://dx.doi.org/10.1007/BF00119502>.
- [38] Oliver T. Schmidt, Tim Colonius, Guide to spectral proper orthogonal decomposition, *AIAA J.* (ISSN: 00011452) 58 (3) (2020) 1023–1033, <http://dx.doi.org/10.2514/1.J058809/ASSET/IMAGES/LARGE/FIGURE8.JPEG>, URL <https://arc.aiaa.org/doi/10.2514/1.J058809>.
- [39] Akhil Nekkanti, Oliver T. Schmidt, Frequency–time analysis, low-rank reconstruction and denoising of turbulent flows using SPOD, *J. Fluid Mech.* (ISSN: 1469-7645) 926 (2021) <http://dx.doi.org/10.1017/jfm.2021.681>.
- [40] J.L. Lumley, in: A.M. Yaglom, V.I. Tartarsky (Eds.), *The Structure of Inhomogeneous Turbulent Flows*, 1967.
- [41] John L. Lumley, *Stochastic Tools in Turbulence*, Dover Publications, 1970.
- [42] Peter D. Welch, The use of fast Fourier transform for the estimation of power spectra: A method based on time averaging over short, modified periodograms, *IEEE Trans. Audio Electroacoust.* (ISSN: 00189278) 15 (2) (1967) 70–73, <http://dx.doi.org/10.1109/TAU.1967.1161901>.
- [43] Oliver T. Schmidt, Spectral proper orthogonal decomposition using multitaper estimates, *Theor. Comput. Fluid Dyn.* (ISSN: 14322250) 36 (5) (2022) 741–754, <http://dx.doi.org/10.1007/S00162-022-00626-X>.
- [44] L. Kristensen, N.O. Jensen, Lateral coherence in isotropic turbulence and in the natural wind, *Bound.-Layer Meteorol.* (ISSN: 15731472) 17 (3) (1979) 353–373, <http://dx.doi.org/10.1007/BF00117924/METRICS>, URL <https://link.springer.com/article/10.1007/BF00117924>.
- [45] Etienne Cheynet, *Wind-Induced Vibrations of a Suspension Bridge: A Case Study in Full-Scale Ph.D. thesis*, University of Stavanger, 2016, URL <https://uis.braage.unit.no/uis-xmlui/handle/11250/2425472>.
- [46] Donald H. Lenschow, B. Boba Stankov, Length scales in the convective boundary layer, *J. Atmos. Sci.* 43 (12) (1986) 1198–1209, [http://dx.doi.org/10.1175/1520-0469\(1986\)043<1198:LSITCB>2.0.CO;2](http://dx.doi.org/10.1175/1520-0469(1986)043<1198:LSITCB>2.0.CO;2), URL [https://journals.ametsoc.org/view/journals/atsc/43/12/1520-0469\\_1986\\_043\\_1198\\_lsitcb\\_2\\_0\\_co\\_2.xml](https://journals.ametsoc.org/view/journals/atsc/43/12/1520-0469_1986_043_1198_lsitcb_2_0_co_2.xml).
- [47] Rudolf O. Weber, Remarks on the definition and estimation of friction velocity, *Bound.-Layer Meteorol.* (ISSN: 00068314) 93 (2) (1999) 197–209, <http://dx.doi.org/10.1023/A:1002043826623/METRICS>, URL <https://link.springer.com/article/10.1023/A:1002043826623>.

- [48] Pingzhi Fang, Wendong Jiang, J.I.E. Tang, Xiaotu Lei, Jianguo Tan, Variations in friction velocity with wind speed and height for moderate-to-strong onshore winds based on measurements from a coastal tower, *J. Appl. Meteorol. Climatol.* (ISSN: 1558-8424) 59 (4) (2020) 637–650, <http://dx.doi.org/10.1175/JAMC-D-18-0327.1>, URL <https://journals.ametsoc.org/view/journals/apme/59/4/jamc-d-18-0327.1.xml>.
- [49] P.M.O. Gebraad, M.J. Churchfield, P.A. Fleming, Incorporating atmospheric stability effects into the FLORIS engineering model of wakes in wind farms, *J. Phys. Conf. Ser.* 753 (5) (2016) 52004, <http://dx.doi.org/10.1088/1742-6596/753/5/052004>.
- [50] R. Courant, K. Friedrichs, H. Lewy, Über die partiellen differenzengleichungen der mathematischen physik, *Math. Ann.* (ISSN: 00255831) 100 (1) (1928) 32–74, <http://dx.doi.org/10.1007/BF01448839/METRICS>, URL <https://link.springer.com/article/10.1007/BF01448839>.
- [51] Eliot Quon, Matthew Churchfield, Lawrence Cheung, Stefan Kern, Development of a wind plant large-eddy simulation with measurement-driven atmospheric inflow, in: American Institute of Aeronautics and Astronautics SciTec, Grapevine, Texas, 2017, URL <http://www.osti.gov/scitech>.
- [52] R. Thedin, E. Quon, M. Churchfield, P. Veers, Investigations of correlation and coherence in turbulence from a large-eddy simulation, *Wind Energy Sci.* 8 (4) (2023) 487–502, <http://dx.doi.org/10.5194/wes-8-487-2023>, URL <https://wes.copernicus.org/articles/8/487/2023/>.
- [53] Hauke Wurps, Gerald Steinfeld, Stefan Heinz, Grid-resolution requirements for large-eddy simulations of the atmospheric boundary layer, *Bound.-Layer Meteorol.* (ISSN: 15731472) 175 (2) (2020) 179–201, <http://dx.doi.org/10.1007/S10546-020-00504-1/TABLES/5>, URL <https://link.springer.com/article/10.1007/s10546-020-00504-1>.
- [54] IEC 61400-3-1:2019 | IEC Webstore, International Electrotechnical Commission (IEC), URL <https://webstore.iec.ch/publication/29360>.
- [55] A.S. Monin, A.M. Obukhov, Basic laws of turbulent mixing in the surface layer of the atmosphere, *Geophys. Inst. Acad. Sci. USSR* 24 (151) (1954) 163–187, URL [https://gibbs.science/efd/handouts/monin\\_obukhov\\_1954.pdf](https://gibbs.science/efd/handouts/monin_obukhov_1954.pdf).
- [56] Bowen Zhou, Fotini Katopodes Chow, Turbulence modeling for the stable atmospheric boundary layer and implications for wind energy, *Flow Turbul. Combust.* (ISSN: 13866184) 88 (1–2) (2012) 255–277, <http://dx.doi.org/10.1007/S10494-011-9359-7/METRICS>, URL <https://link.springer.com/article/10.1007/s10494-011-9359-7>.
- [57] Delft High Performance Computing Centre (DHPC), DelftBlue supercomputer (phase 2), 2024, URL <https://www.tudelft.nl/dhpc/ark:/44463/DelftBluePhase2>.
- [58] AAM Holtslag, G Svensson, P Baas, S Basu, B Beare, ACM Beljaars, FC Bosveld, J Cuxart, J Lindvall, GJ Steeneveld, M Tjernström, BJH Van De Wiel, Stable atmospheric boundary layers and diurnal cycles: Challenges for weather and climate models, *Bull. Am. Meteorol. Soc.* 94 (11) (2013) 1691–1706, <http://dx.doi.org/10.1175/BAMS-D-11-00187.1>.
- [59] Shengbai Xie, Cristina L. Archer, A numerical study of wind-turbine wakes for three atmospheric stability conditions, *Bound.-Layer Meteorol.* (ISSN: 1573-1472) 165 (1) (2017) 87–112, <http://dx.doi.org/10.1007/s10546-017-0259-9>.
- [60] Gerard Schepers, Pim Van Dorp, Remco Verzijlbergh, Peter Baas, Harmen Jonker, Aeroelastic loads on a 10MW turbine exposed to extreme events selected from a year-long large-eddy simulation over the North Sea, *Wind Energy Sci.* (ISSN: 23667451) 6 (4) (2021) 983–996, <http://dx.doi.org/10.5194/WES-6-983-2021>.
- [61] E Branlard, B Jonkman, GR Pirrung, K Dixon, J Jonkman, Dynamic inflow and unsteady aerodynamics models for modal and stability analyses in OpenFAST, in: TORQUE 2022: Journal of Physics: Conference Series, Vol. 2265, IOP Publishing, 2022, <http://dx.doi.org/10.1088/1742-6596/2265/3/032044>, URL <https://www.nrel.gov/docs/fy22osti/82343.pdf>.
- [62] Rick Damiani, Greg Hayman, The unsteady aerodynamics module for FAST 8, NREL Tech. Rep. (2019) URL <https://www.nrel.gov/docs/fy20osti/66347.pdf>.
- [63] NREL, ROSCO toolbox, 2021, GitHub repository. URL <https://github.com/NREL/ROSCO>.
- [64] Tamino Wetz, Josef Zink, Jens Bange, Norman Wildmann, Analyses of spatial correlation and coherence in ABL flow with a fleet of UAS, *Bound.-Layer Meteorol.* (ISSN: 15731472) 187 (3) (2023) 673–701, <http://dx.doi.org/10.1007/S10546-023-00791-4/FIGURES/14>, URL <https://link.springer.com/article/10.1007/s10546-023-00791-4>.
- [65] L. Kristensen, N.O. Jensen, E.L. Petersen, L. Kristensen, N.O. Jensen, E.L. Petersen, Lateral dispersion of pollutants in a very stable atmosphere—the effect of meandering, *AtmEn* (ISSN: 1352-2310) 15 (5) (1981) 837–844, [http://dx.doi.org/10.1016/0004-6981\(81\)90288-2](http://dx.doi.org/10.1016/0004-6981(81)90288-2), URL <https://ui.adsabs.harvard.edu/abs/1981AtmEn..15..837K/abstract>.
- [66] B.M. Koprov, V.M. Koprov, T.I. Makarova, G.S. Golitsyn, Coherent structures in the atmospheric surface layer under stable and unstable conditions, *Bound.-Layer Meteorol.* (ISSN: 00068314) 111 (1) (2004) 19–32, <http://dx.doi.org/10.1023/B:BOUN.0000010996.99753.D3/METRICS>, URL <https://link.springer.com/article/10.1023/B:BOUN.0000010996.99753.d3>.
- [67] Astrid Nybø, Finn Gunnar Nielsen, Marte Godvik, Quasi-static response of a bottom-fixed wind turbine subject to various incident wind fields, *Wind Energy* (ISSN: 1099-1824) 24 (12) (2021) 1482–1500, <http://dx.doi.org/10.1002/WE.2642>, URL <https://onlinelibrary.wiley.com/doi/full/10.1002/we.2642>.
- [68] Amy N. Robertson, Kelsey Shaler, Latha Sethuraman, Jason Jonkman, Sensitivity analysis of the effect of wind characteristics and turbine properties on wind turbine loads, *Wind Energy Sci.* (ISSN: 23667451) 4 (3) (2019) 479–513, <http://dx.doi.org/10.5194/WES-4-479-2019>.
- [69] A Sathe, J Mann, T Barlas, W.A.A.M. Bierbooms, GJW van Bussel, Influence of atmospheric stability on wind turbine loads, *Wind Energy* 16 (7) (2013) 1013–1032, <http://dx.doi.org/10.1002/we.1528>.
- [70] Ameya Sathe, Wim Bierbooms, Influence of different wind profiles due to varying atmospheric stability on the fatigue life of wind turbines, *J. Phys. Conf. Ser.* (ISSN: 1742-6596) 75 (1) (2007) 012056, <http://dx.doi.org/10.1088/1742-6596/75/1/012056>.
- [71] Tobias Günther, Markus Gross, Holger Theisel, Generic objective vortices for flow visualization, *ACM Trans. Graph.* (ISSN: 0730-0301) 36 (4) (2017) <http://dx.doi.org/10.1145/3072959.3073684>.
- [72] S. Popinet, Free computational fluid dynamics, *ClusterWorld* 2 (6) (2004) URL <http://gfs.sf.net/> <https://cgl.ethz.ch/research/visualization/data.php>.
- [73] C.H.K. Williamson, G.L. Brown, A series to represent the strouhal-Reynolds number relationship of the cylinder wake, *J. Fluids Struct.* 12 (1998) 1073–1085, <http://dx.doi.org/10.1006/jfls.1998.0184>.
- [74] Robert J. Beare, Malcolm K. Macvean, Albert A.M. Holtslag, Joan Cuxart, Igor Esau, Jean Christophe Golaz, Maria A. Jimenez, Marat Khairoutdinov, Branko Kosovic, David Lewellen, Thomas S. Lund, Julie K. Lundquist, Anne McCabe, Arnold F. Moene, Yign Noh, Siegfried Raasch, Peter Sullivan, An intercomparison of large-eddy simulations of the stable boundary layer, *Bound.-Layer Meteorol.* (ISSN: 00068314) 118 (2) (2006) 247–272, <http://dx.doi.org/10.1007/S10546-004-2820-6/METRICS>, URL <https://link.springer.com/article/10.1007/s10546-004-2820-6>.
- [75] Björn Maronga, Dan Li, An investigation of the grid sensitivity in large-eddy simulations of the stable boundary layer, *Bound.-Layer Meteorol.* (ISSN: 15731472) 182 (2) (2022) 251–273, <http://dx.doi.org/10.1007/S10546-021-00656-8/FIGURES/11>, URL <https://link.springer.com/article/10.1007/s10546-021-00656-8>.
- [76] Lars Davidson, Large eddy simulations: How to evaluate resolution, *Int. J. Heat Fluid Flow* (ISSN: 0142-727X) 30 (5) (2009) 1016–1025, <http://dx.doi.org/10.1016/j.ijheatfluidflow.2009.06.006>, URL <https://www.sciencedirect.com/science/article/pii/S0142727X09001039>.